Ferromagnetic Resonance Spectroscopy of Arrays of Coupled Nanomagnets

A Dissertation

Presented to

the Faculty of the Materials Science and Engineering Program

University of Houston

In Partial Fulfillment

of the Requirements for the Degree

Doctor of Philosophy

in Materials Science and Engineering

by

Ivan Nekrashevich

December 2016

Ferromagnetic Resonance Spectroscopy of Arrays of Coupled Nanomagnets

Ivan Nekrashevich

Approved:

Chair of the Committee
Dr. Dmitri Litvinov, Professor
Materials Science and Engineering
Electrical and Computer Engineering

Committee Members:

Dr. Vassiliy Lubchenko, Associate Professor
Chemistry

Dr. Paul Ruchhoeft, Associate Professor
Materials Science and Engineering

Dr. Jiming Bao, Associate Professor
Materials Science and Engineering

Dr. Stanko Brankovic, Associate Professor
Materials Science and Engineering

Dr. Suresh K. Khator, Associate Dean
Cullen College of Engineering

Dr. Pradeep Sharma, Professor and Director
Materials Science and Engineering

Acknowledgement

I would like to thank Professors Dmitri Litvinov and Paul Ruchhoeft who supervised my research from its conception through the final stages.

Also I would like to acknowledge the contributions to this work made by Professor James Rantschler who provided great help and leadership in initial setup of ferromagnetic resonance spectrometer and helped to clarify certain questions regarding magnetization dynamics in thin films and multilayers. I would like to acknowledge contributions of Alexey Kaplan who provided help on the early stages of described herein project.

I’m very thankful to Dr. Long Chang for providing me with valuable advices on nanofabrication and characterization techniques and insightful conversations that covered the topic of my research and beyond.

Ferromagnetic Resonance Spectroscopy of Arrays of Coupled Nanomagnets

An Abstract
of a

Dissertation

Presented to

the Faculty of the Materials Science and Engineering Program

University of Houston

In Partial Fulfillment

of the Requirements for the Degree

Doctor of Philosophy

in Materials Science and Engineering

by

Ivan Nekrashevich

December 2016

Abstract

Magnetodynamic properties of large area magnetic nanopatterns are of the great interest for magnetic hard drive storage industry and novel magnetic logic devices. With general trend for miniaturization and increase of areal density of magnetic nanodevices, collective magnetodynamic behavior will play increasingly important role. Thus, understanding and identification of the key factors affecting performance of coupled nanomagnetic system is the crucial part in the future success of magnetism related industries. In this work, we look at phenomena of ferromagnetic and spin wave (SW) resonances in magnetic nanopatterned films. Also, within the scope of this study are conditions of emergence, magnetic properties, and stability of the magnetic vortices in large arrays of $Ni_{19}Fe_{81}$ (permalloy) dipole coupled nanomagnets.

In our experimental studies, we survey magnetodynamic properties and magnetic texture of permalloy nanopatterns by means of the field sweep FMR spectrometry, Alternating Gradient Field Magnetometry, Polar Magneto-Optical Kerr Effect Magnetometry, and Magnetic Force Microscopy. Using electron-beam lithography and lift-off process, we fabricate and characterize magnetic nanopatterned films with a wide range of geometrical parameters such as lateral size of rectangular nanomagnets, nanomagnet aspect ratio and the duty cycle of the square pattern as well as type of 2D lattice. By changing the geometrical parameters of the nanostructures we achieve control over the ferromagnetic and spin-wave resonance modes in patterned films at various directions of external bias magnetic field. Using FMR spectrometry, we measure the

critical angles between the DC magnetic field and the plane of the nanopattern at which quantized standing spin wave modes are excited (resonance mode splitting).

Our experimental results were supplemented with analytic calculations and micromagnetic simulations. Proposed analytic model allows distinguishing between the observed resonance modes based on effective demagnetizing factors which in their turn represent geometries of individual nanomagnets and geometrical properties of arrays. Our micromagnetic simulations are in good agreement with experimental observations and confirm our assumptions about significant contribution of long range dipolar interdot coupling to magnetic textures and spin wave resonance spectrum of nanodot arrays.

Table of Contents

List of Figures

Chapter 1. Introduction

1.1 Motivation

Experts from International Data Corp. and Western Digital Corp. predict that data storage capacity demanded by the global market in year 2020 will reach approximately 2900 exabytes (1 EB = 1 million TB), it is almost three times higher comparing to around 1000 EB in 2015. There are several various factors that drive the demand for ever increasing data storage capacity, among these factors are Big Data, Internet-of-Things, user-generated content, enterprise storage, personal storage and so on. Samsung Electronics, one of the major manufacturers of solid state-based electronics, projects that the NAND flash industry will deliver about 253 EB of flash memory in 2020, approximately four times higher total volume comparing to 84 EB in 2015. Thus, various types of solid-state storage will account for less than 10% of the total volume of storage market in terms of bytes provided, whereas technologies assumed to be traditional, such as hard drives, tape and some other account for over 90%, if the estimates by IDC, Samsung and Western Digital are correct. According to predictions of Western Digital analysts the segmentation of the data storage demand will also change considerably by the year 2020 with the PC market demand giving a way to the faster growing enterprise market segment, see Figure 1.1.

It is very unlikely that exponential growth trend in data storage demand observed over the last five decades will change in the nearest future. Yet to satisfy this demand the

industry has to overcome certain fundamental limitations of the current data storage technology. This will require development of new qualitatively different approaches for data read and write processes as well as development of novel suitable materials.

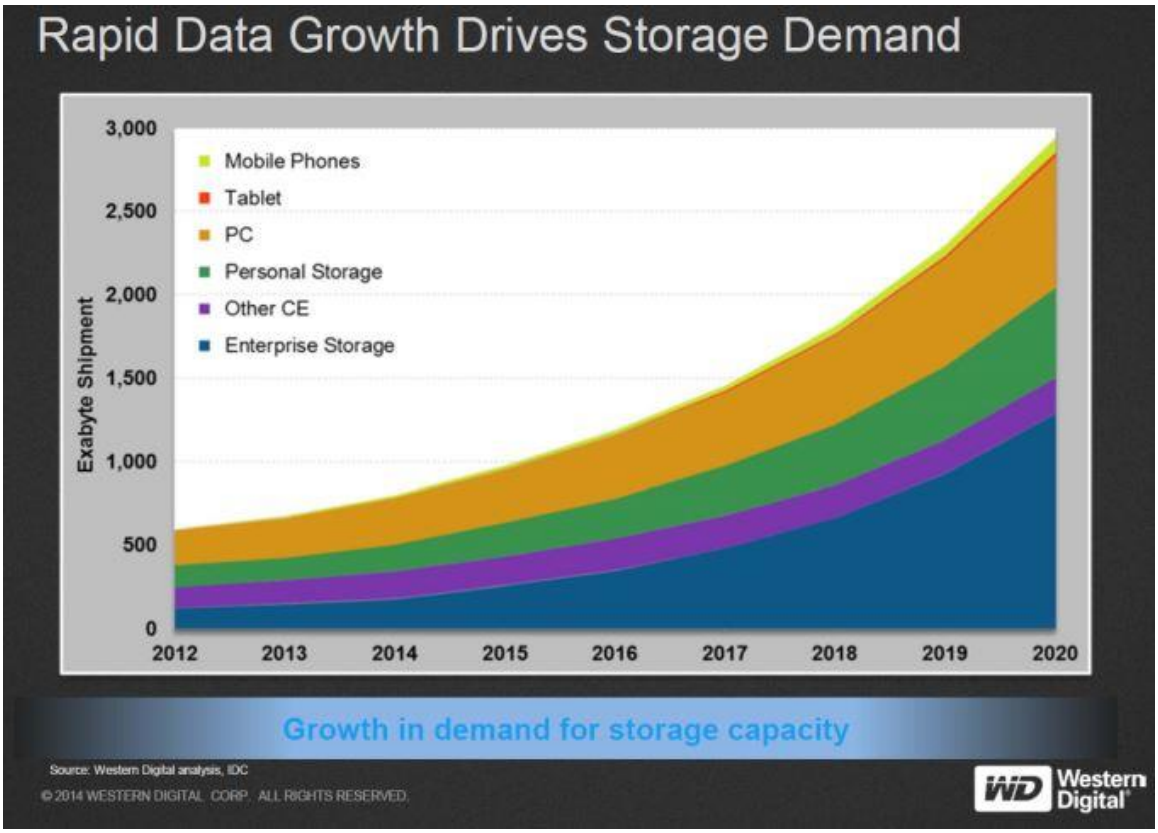

Figure 1.1 Projected data storage market capacity and segmentation by various types of consumers. Image is the courtesy of Western Digital Corporation.

1.2 Magnetic Data Storage Overview and Limitations

The idea of storing data using magnetic media is almost 130 years old. The first proposal to use cotton or silk threads imbued with steel dust or short clippings of fine wire for sound recording was made by Oberlin Smith as early as 1888. The first working magnetic recording device was produced 10 years later in 1898 by Valdemar Poulsen. In

this device a signal was recorded on a magnetic wire wrapped around a drum. This technological solution can be considered as a predecessor of magnetic tape recording devices.

In a broader view, ferromagnetic materials are favorable for data storage applications due to their ability to retain the magnetized state initially set by the writing/magnetizing device over long periods of time, accessibility and relative low cost of the materials themselves. This quality overshadows electric charge-based devices due to their tendency to leak, dissipate charge and produce unwanted electric field interfering with other electronic components of a recording system. Besides that, generated stray magnetic field flux is relatively easily converted to electric signals that can later be transmitted and/or processed by electronic devices and written back onto a data storage media. Such conversion was initially done by means of induction coils and later, in modern devices, using giant or tunnel magnetoresistive sensors, GMR and TMR respectively.

In general, digital or analog information is written to and read from a storage medium as it moves past devices called read-and-write heads. In some devices read and write heads are separated. Read-and-write heads typically operate very close (often tens of nanometers or less) to the surface of magnetic medium. The read-and-write head is used to detect and modify or flip the magnetization of the magnetic recording material immediately under it. In case of digital data storage, there are two magnetic polarities, each of which is used to represent either 0 or 1.

The first hard disk drives (HDD) used longitudinal magnetic recording concept where magnetization of each uniformly magnetized region is confined to the direction

parallel to thin magnetic film. Later, in mid 2000s, this approach was succeeded by perpendicular magnetic recording (PMR) concept, where the magnetization of the regions encoding logical 0s and 1s (magnetization pointing up and down, respectively, or vice versa) is directed normal to the plane of the magnetic layer. This approach allowed for considerable improvement of the areal recording density (usually measured in bits per square inch) thus allowing to store more data on a device with the same geometrical parameters/constrains, see Figure 1.2.

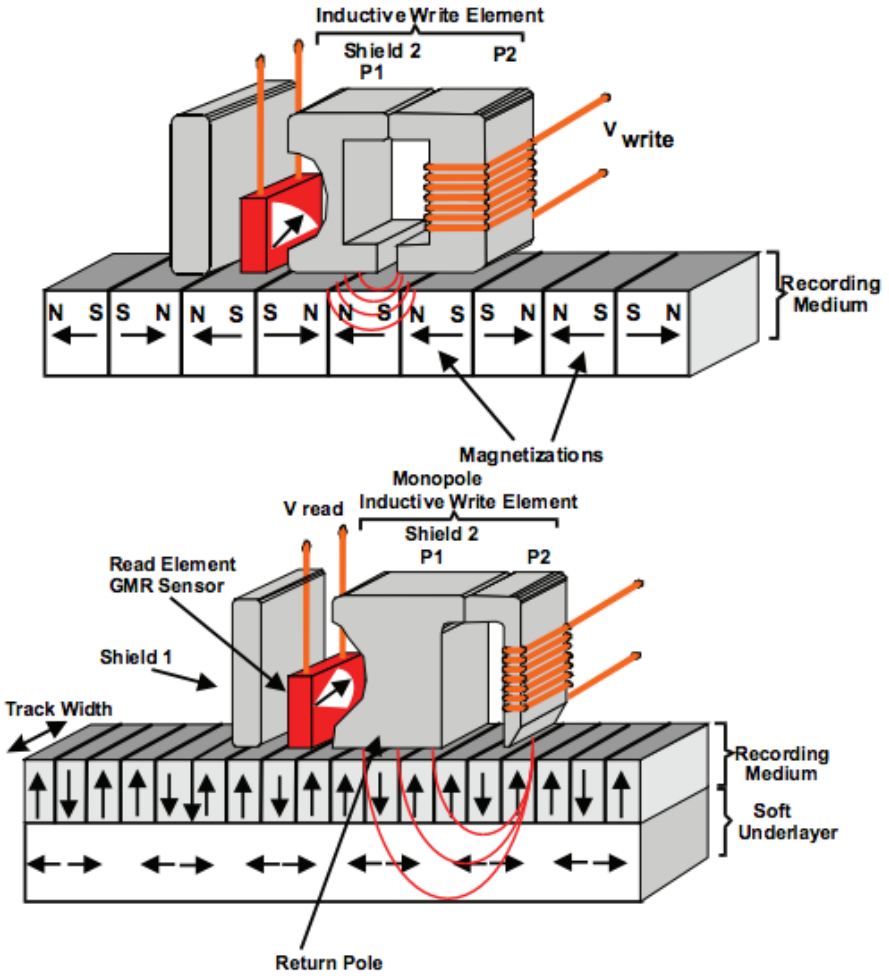

Figure 1.2 Schematic representations of the longitudinal (top) and perpendicular (bottom) magnetic recording processes [1].

Comparing the two recording approaches shown on the Figure 1.2 it can be noted that the geometry of the return flux pole of the PMR read-and-write head (P1 and P2) has changed allowing to generate higher more geometrically confined write fields. Another addition in PMR head is the soft magnetic underlayer lying below the main data recording layer. Due to its "softness" i.e. high susceptibility to external magnetic fields, this underlayer readily conducts magnetic flux. When the write head is magnetized by the induction coils of the pole P2, flux concentrates under the small wedge-shaped pole-tip and generates an intense magnetic field in the short gap between the pole-tip and soft underlayer. The recording layer that stores the data is directly in this gap where the field is most intense. The soft underlayer in this case works as a mirror for magnetic flux thus effectively increasing the applied writing magnetic field. Ability to generate higher writing fields allows for higher coercivity media to be used. Such media require higher fields to set the magnetization, but once set, the magnetization is inherently more stable.

The presence of the soft underlayer and its "mirroring" properties also increase the amplitude of the readback signals and helps decrease interference from adjacent tracks. Although the read head itself did not undergo significant changes, the waveforms that come out of the head are quite different and require new signal processing techniques such as partial response maximum likelihood (PRML) channel optimization in order to gain the most benefit.

In retrospect, after deployment of the first hard disk drives used in the RAMAC 305 computers in 1956, development of magnetic data storage technology can be described as rapid evolution. During this time the conceptual design of the HDDs didn't experience major changes. The main improvements were done in optimization of the

read-and-write head and media materials as well as head parts miniaturization and improvements of the electronic and mechanical components. The basic concepts stayed the same. However, during this time, HDD industry saw the exponential growth in data storage density doubling hard drive capacity almost every year and matching the rate of transistor density observed in the semiconductor industry, so called Moore's law. Looking at the drive such as the one used in RAMAC 305 computers weighting more than a ton, it could store about 5 megabytes (5×10^6 bytes) of data at the cost of about $10,000,000 per gigabyte to the modern HDD devices, 1.72 pounds, storing more than 8 terabytes (8×10^{12} bytes) at a cost of $0.03 per gigabyte. Since its invention, the HDD has become approximately 8,500 times smaller, 1,000 times lighter, 100 million times cheaper and storing about 10 million times more information. Such numbers are unprecedented and unmatched by any other industry.

It is natural to suppose that such rapid growth cannot continue forever without need for the major design overhaul concerning the basics of magnetic recording. And indeed such requirement has arisen in the view of the superparamagnetic challenge – a fundamental limitation for both longitudinal and perpendicular magnetic data storage technologies.

Ferromagnetic materials are known for their ability to retain their magnetization for extended periods of time after the magnetizing field was removed. This is assumed under the condition that temperature of the material is below the ferromagnet-paramagnet phase transition temperature, called Curie temperature. However, when the volume of the magnet becomes sufficiently small, typically on the order of 100 nm or less, the magnetization of such structured material starts to oscillate randomly switching

directions. Such behavior is caused by thermal fluctuations. For examples of superparamagnetic nanoparticles, see Figures 1.3 and 1.4. In case of superparamagnetic particle magnetization averaged even over relatively short time will become almost zero. This phenomenon is called the superparamagnetic limit, and the information stored in a state of superparamagnetic domain is lost over short period of time, rendering such media ineffective.

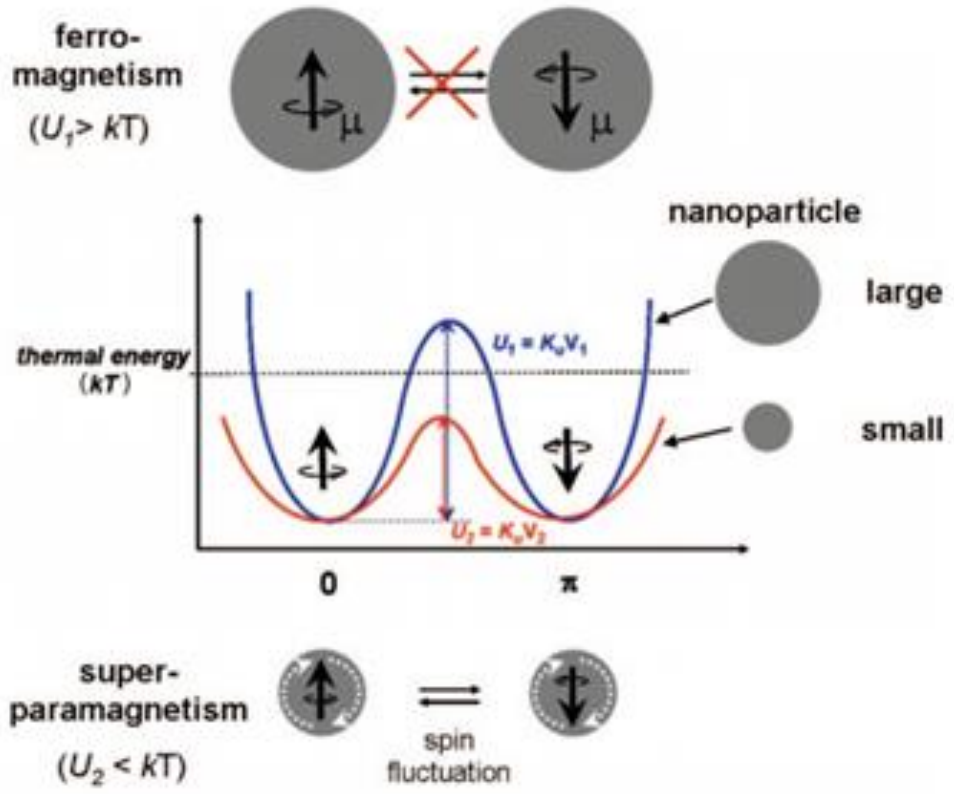

Figure 1.3 Nanoscale transition of magnetic nanoparticles from ferromagnetic to superparamagnetic state.

Figure 1.3 shows schematic energy diagram of magnetic nanoparticles with different magnetic spin alignment, showing ferromagnetism in a large particle (top) and superparamagnetism in a small nanoparticle (bottom) [2].

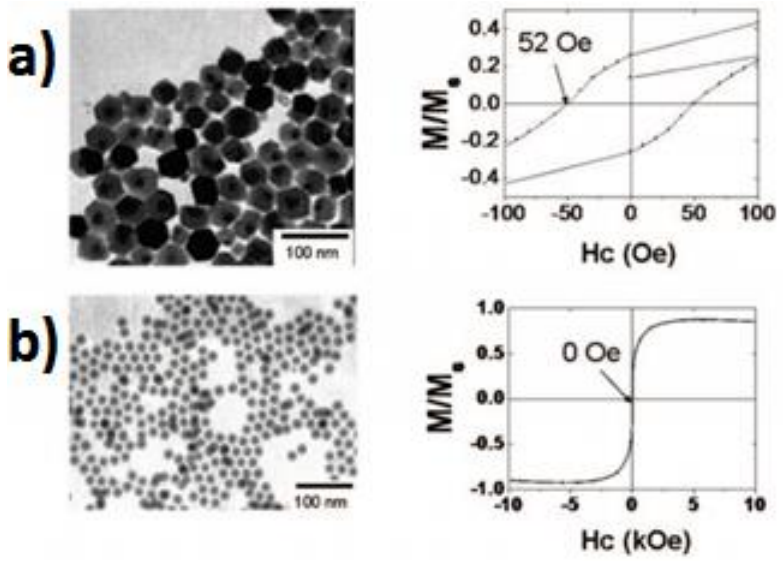

Figure 1.4 Size dependent transition of iron oxide nanoparticles from superparamagnetism to ferromagnetism.

Figure 1.4 shows the size dependent transition of iron oxide nanoparticles from superparamagnetism to ferromagnetism with transmission electron microscope (TEM) images (left) and hysteresis loops of (a) 55 nm and (b) 12 nm sized iron oxide nanoparticles (right) [2]. Normalized magnetization loops show significant reduction of coercivity observed in 12 nm nanoparticles. Such behavior is typical for superparamagnetic transition.

The mean time between the two states of spontaneous magnetization reversal of a ferromagnetic particle is given by Neel-Arrhenius equation:

$$t = \frac{1}{f_0} \exp\left(\frac{K_u V}{k_B T}\right), \tag{1.1}$$

where t is the switching time, f_0 is the attempt frequency, typically in the range from 1 GHz to 10 GHz, K_u is the material specific magnetic anisotropy constant of the grain, V is the volume, k_B is the Boltzmann constant, and T is the temperature. When engineering a hard drive, it is typical to set the switching time to approximately ten years and engineer materials to achieve the appropriate performance. Analyzing equation (1.1) one can see that the size of a particle and its temperature play similar roles for the stability of magnetization. For instance, if the measurement time t is fixed, gradual increase in temperature will cause initially stable ferromagnetic particle to transform to superparamagnetic state. The temperature when this transition occur is called blocking temperature of the given material. Similarly, if instead temperature is fixed and the size of the particle is varied, it will undergo superparamagnetic transition. Thus superparamagnetic transition characterized by the measurement procedure, material properties, temperature and size of the magnetic system. It is important to note that this is not a physical phase transition, where order parameter of a system changes.

Dimensionless figure of merit for magnetic data storage applications is the ratio $\frac{K_u V}{k_B T}$ which should be greater than ~60 to ensure the stability of saved data over 10 year period of time at room temperature and typical values of magnetic anisotropy and magnetic bit size. Superparamagnetic limit causes so called magnetic recording trilemma.

As we showed above, thermal stability of a bit of information is of critical importance particularly as bits are made smaller and media are made thinner. In conventional longitudinal and perpendicular magnetic recording, the medium presented by a granular film and a bit consists of several tens ($N \cong 20 \div 30$) almost non-interacting magnetic grains separated by thin layers of oxide at the grain boundaries. In general, read

signal-to-noise ratio (SNR) is complex to derive and depends on factors such as the shape of bits and cross-talk between neighboring bits or even neighboring tracks but from simple statistical estimation SNR is proportional to $\sqrt{N}$ [3]. Therefore, the number of grains included in a bit cannot be significantly reduced in order to preserve SNR and, consequently, the increasing bit density implies a reduction of the grain size. However, a reduction in the grain size leads to a reduction in the energy barrier K_uV (see Figure 1.3 (a) and equation (1)) that is separating two magnetization states which determines the thermal stability of the written information. Thus, choice of materials with high anisotropy K_u is required to regain thermal stability which in its turn requires higher fields to flip magnetization of a bit to write information. Described above situation was called magnetic recording trilemma as to achieve the result it requires adjustment of three mutually conflicting parameters, see Figure 1.5.

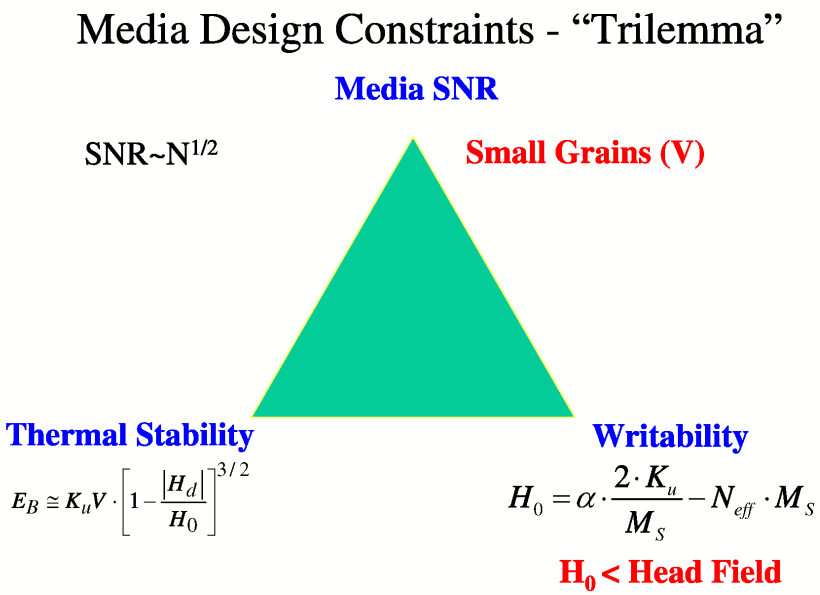

Figure 1.5 Mutually excluding requirements composing the magnetic recording trilemma. Here the effects of demagnetizing and coercive field taken in account for thermal stability and writability.

Facing the challenge of superparamagnetic limit, several approaches were put forward by research community. Among the most promising is Shingled Magnetic Recording (SMR) – already implemented but provides only short term solution; Energy Assisted Magnetic Recording – a group of approaches including Heat Assisted Magnetic Recording (HAMR) and Microwave Assisted Magnetic Recording (MAMR); Bit Patterned Media (BPM) Recording.

Let us examine the MAMR in greater detail as we will further develop this approach in this dissertation. Initially MAMR concept was introduced in 2008 by Jian-Gang Zhu and his colleagues from Carnegie Mellon University [4]. The idea is to utilize the ferromagnetic resonance phenomenon to assist in flipping of magnetization of a magnetic domain with uniaxial anisotropy. Figure 1.6 shows a calculated magnetization trajectory of a $6 \times 6 \times 6$ nm magnetic grain with a uniaxial anisotropy via micromagnetic simulation that utilizes the Landau–Lifshitz–Gilbert equations with a Gilbert damping constant $\alpha = 0.02$. A pulsed magnetic field with a pulsewidth of 1 ns, a rise time of 0.2 ns, and an amplitude of $0.5H_k$, where H_k is the anisotropy field of the grain, is applied along the vertical easy axis opposite to the initial magnetization. An AC field of an amplitude $0.1H_k$ is applied along the direction perpendicular to the vertical easy axis at an angular frequency $\omega = 0.45\gamma H_k$, where γ is the gyromagnetic ratio. Without the AC field, applied reversing field of $0.5H_k$ will not be enough to flip the magnetic bit and the magnetization of the grain will remain static along the easy axis in the initial direction. With the presence of the ac field, the magnetization precession will increase its precessional angle and irreversibly gyro downwards within the duration of the pulsed reversing field.

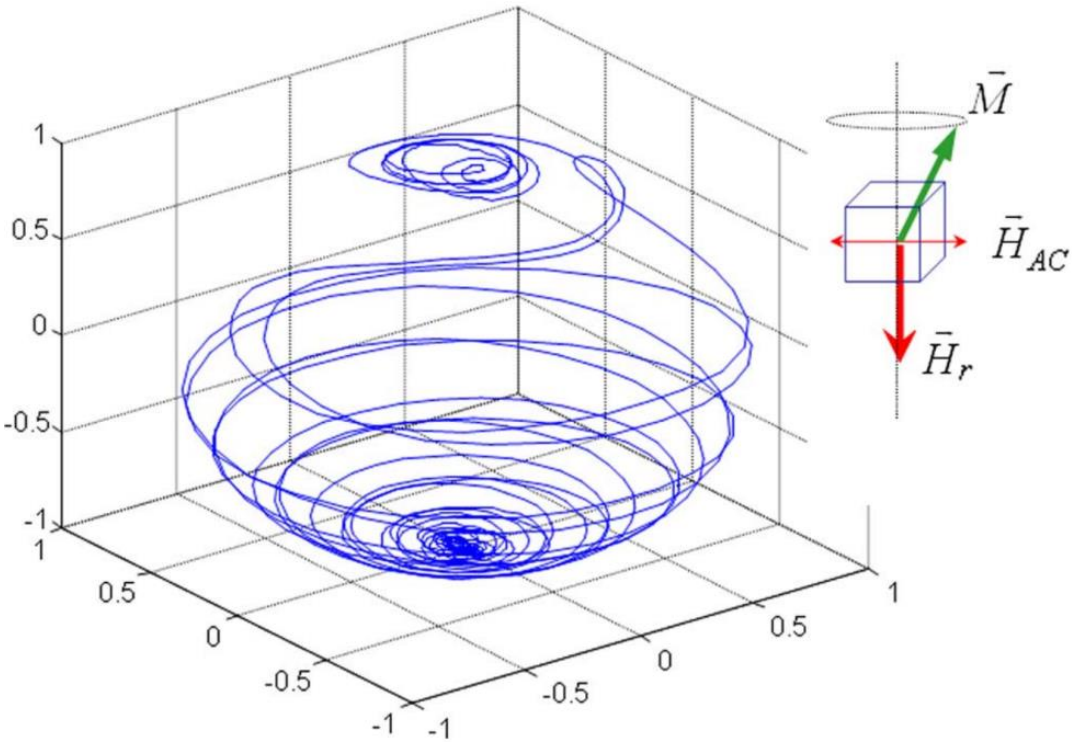

Figure 1.6 Calculated trajectory of volume-averaged magnetization of a magnetic grain with uniaxial anisotropy in the presence of a transverse AC field. The reversing field H is $0.5H_k$.

On the Figure 1.6, the AC field is at the angular frequency of $\omega = 0.45\gamma H_k$, with the amplitude of $0.1H_k$. The trajectory shown on is over 2 ns thime duration, starting from the rise of reversing field pulse.

In the described above system, if the frequency of the transverse AC field matches the ferromagnetic resonance frequency of the grain, which is determined by the externally applied reversing field and the anisotropy field of the grain, the system will absorb energy from the AC field. If the rate of the energy absorption exceeds the rate of damping, the magnetization precession amplitude will increase with time, eventually leading to an irreversible magnetization flip if the reversing field applied for sufficiently long time.

The described herein work on magnetization dynamics in arrays of nanomagnets can be used for realization of a hybrid approach combining MAMR and BPM technologies. In this case the magnetic recording medium is formed by an array of separated grains of magnetic material that do not have common boundaries. Magnetization of each of the single domain grains represents a single bit encoding logical 0 or 1. For comparison with conventional media, see Figure 1.7. In the hybrid approach the magnetization reversal is done by means of MAMR, described earlier.

Besides applications for magnetic data storage and MAMR, magnetization dynamics gained significant interest as an essential part of the young research fields of spintronics and magnonics.

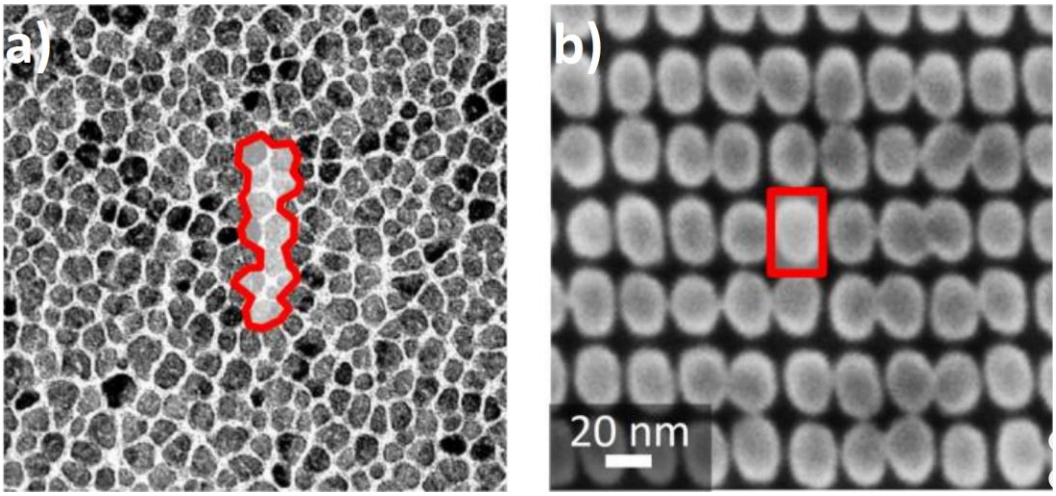

Figure 1.7 Comparison of (a) conventional and (b) bit patterned media. On granular media, an individual bit is recorded on an ensemble of grains (red outline), on bit patterned media, each island stores one bit [5].

In spintronics, in addition to manipulation of electron charge to store and process information, an additional degree of freedom is used – electron spin. Conventional electronic devices rely on electron charge to transport and store information, spintronic devices in addition rely on its spin. Most spintronic devices operate according to the

following scheme: 1) information is stored (written) into a group of electron spins as a particular magnetization orientation, 2) polarized spins carry the information along a conducting channel and 3) the information is read at a terminal. Thus magnetic states of a system can be controlled with both electric and magnetic fields. Spin orientation of conduction electrons survives for a relatively long time (nanoseconds, compared to tens of femtoseconds during which electron momentum decays due to scattering), which makes spintronic devices particularly attractive for memory storage and magnetic sensors applications, and, potentially for quantum computing where spin of single electron represents a bit (called qubit) of information.

Magnonics comprises the study of excitation, detection, and manipulation of magnons. Spin waves or magnons are phase-coherent precessions of microscopic vectors of magnetization of the magnetic medium and can be considered as weakly interacting quasi particles obeying Bose-Einstein statistics, Figure 1.8. In regard to applications, magnonic devices rely on a quanta of magnetization excitation – a spin wave or magnon for information manipulation. Spin-waves can of both types: propagating and standing depending on the conditions imposed by the magnetic media. Spin-wave caring media with specially engineered magnetic properties called magnonic crystal.

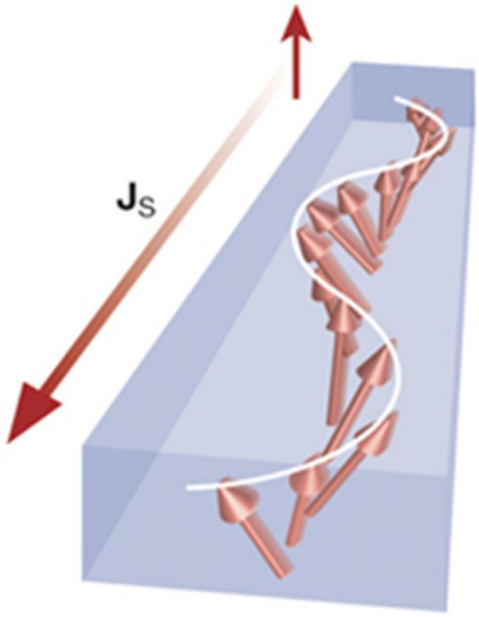

Figure 1.8 A schematic illustration of a spin-wave spin current: spin angular momentum carried by collective magnetic-moment precession. Spin angular momentum J_s carried by a spin-wave [6].

1.3 Preliminaries

Ferromagnetic resonance (FMR) is a phenomenon of resonant absorption of external electromagnetic radiation (usually microwave) by ferromagnetic materials due to the collective excitations of magnetic order in ferromagnetic solids. FMR was discovered as early as 1911 by V.K. Arkad'ev when he observed the absorption of high frequency radiation by ferromagnetic bodies and the first qualitative explanation of the observed effect was proposed by Ya. G. Dorfman in 1923. FMR is closely related to some other similar magnetodynamic effects such as electron paramagnetic resonance and nuclear magnetic resonance. While the phenomenology of these phenomena is similar, the key factors influencing the magnetodynamic spectra are quite different.

FMR spectroscopy covers a wide range of microwave spectra from wavelength of about 1 mm to 10 cm (about 1 GHz to 100 GHz), thus allowing to probe magnetization dynamics in ferromagnetic materials with sub 1 ns time resolution. From the quantum theory of light it follows that in microwave-spectroscopical phenomena there is exchange of fairly small quanta of energy $h\nu$ between the ferromagnetic material and electromagnetic field. This energy scale is even lower than that of infrared spectrum. Yet exactly this quality makes it particularly interesting for the new generation of low energy consuming fast data storage and processing devices.

The basics of FMR phenomena can be examined by using Zeeman effect. For each Zeeman multiplet there are definite sets of possible energy transitions for each pair of levels (i and k) of a given multiplet. The frequencies ν_{ik} of the corresponding quanta absorbed or emitted in these transitions are defined by the well-known formula:

$$\mathrm{h}\nu_{\mathrm{ik}} = \hbar\omega_{\mathrm{ik}} = \mathrm{E_i} - \mathrm{E_k} = \Delta\mathrm{E_{ik,}} \tag{1.2}$$

where $\mathrm{h} = 2\pi\hbar = 6.62607004 \times 10^{-34}\ \mathrm{m^2\ kg\ /\ s}$ is the Plank's constant, $\omega_{\mathrm{ik}} = 2\pi\nu_{\mathrm{ik}}$ is the transition frequency, the value of the energy difference ΔE_{ik} is defined by the formula

$$\Delta\mathrm{E_{ik}} = \mathrm{g}\mu_{\mathrm{B}}\Delta\mathrm{m_{ik}H}, \tag{1.3}$$

where g is the spectroscopic splitting Lande factor, connected to the ratio of the magnetic to the mechanical moment, Δm_{ik} is the difference of the magnetic quantum numbers of

the states i and k respectively of the given multiplet, $\mu_B = \frac{e\hbar}{2mc} \cong 0.927 \times 10^{-20}$ e.m.u. is the Bohr magneton (hare m is the mass, e is the charge of electron and c is the speed of light), H is the applied magnetic field. Combining equations (1.2) and (1.3) we obtain the frequency for the transition i -> k:

$$\omega_{ik} = \frac{g\mu_B}{\hbar} \Delta m_{ik} H. \tag{1.4}$$

The values of the differences Δm_{ik} in (1.3) and (1.4) are not arbitrary and limited by the selection rules which for a dipole radiation take the form $\Delta m_{ik} = 0, \pm 1$. Since all the levels in the given Zeeman multiplet have different magnetic quantum numbers i ≠ k, then in actual fact the only transitions to occur are those with $|\Delta m_{ik}| = 1$. Transitions of the type $\Delta m_{ik} = 0$ have linear polarization along the axis parallel to the field **H**, and transitions with $|\Delta m_{ik}| = 1$ have polarization in a plane at right angles to the vector **H**. Thus high frequency excitation field $\mathbf{H}_{\sim}$ causing transitions inside a given multiplet must be at right angles to the constant magnetization field **H** ($\mathbf{H}_{\sim} \perp \mathbf{H}$). Taking in account the selection rules and using the equations (1.3) and (1.4) and the expression for μ_B we can obtain the relation between the resonant frequency and the external field H:

$$\omega_{res} = \gamma H, \tag{1.5}$$

where $\gamma = \frac{g\mu_B}{\hbar} = g\frac{e}{2mc}$ is the gyromagnetic ratio.

From equation (1.5) it can be seen that to satisfy the resonance conditions we can either fix the frequency ω of the excitation magnetic field and vary the magnitude of the applied magnetic field or choose the other way by fixing the magnetic field H and changing the frequency of excitation and finding the maximum of the microwave absorption. Both of the mentioned techniques are widely used in experimental investigations of magnetization dynamics in ferromagnetic thin films and nanopatterns. In our experiments we use the former approach with an addition of variation of orientation of the direction of external field.

Presented above picture shows only the general dynamic properties of a magnetic top placed in a uniform external magnetic field. In general, there are several additional factors that play crucial role in defining the ferromagnetic resonance structure in ferromagnetic materials. Typical ferromagnet is presented by regular atomic lattices of uncompensated magnetic spins coupled with each other through the short range exchange interaction and long range dipolar interaction. Thus each individual magnetic moment is experiencing not just the externally applied magnetic field but also the effective field produced by its surrounding magnetic spins (demagnetizing field) as well as the exchange coupling to the immediate neighbors in the crystal lattice. Besides the exchange and dipolar interactions that are present in all the ferromagnetic materials, among the important factors defining magnetization dynamics can be magnetocrystalline anisotropy, which depends on the angles between the magnetization direction and the crystal's principal axes, magnetoelasticity, which is a function of the direction of magnetization and the stress.

Certain aspects of motion of a magnetic moment of any object with non-zero magnetization about an external magnetic field are described by Larmor equation for precession:

$$\boldsymbol{\tau} = \frac{\mathrm{d}\mathbf{L}}{\mathrm{dt}} = \gamma \mathbf{m} \times \mathbf{B}, \tag{1.6}$$

where $\boldsymbol{\tau}$ is the vector of the torque acting on a magnetized body, **L** is the vector of angular momentum, **m** is the magnetic dipole moment and **B** is the magnetic induction of external field. Using relation connecting the magnetic dipole moment of electron to its angular momentum $\mathbf{m} = \frac{\mathrm{e}}{2\mathrm{mc}}\mathbf{L}$ and expression for gyromagnetic ratio $\gamma = g\frac{e}{2mc}$ we arrive to the equation for the precession of ideal magnetic top composed of non-interacting electron spins in external magnetic field:

$$\frac{\mathrm{d}\mathbf{M}}{\mathrm{dt}} = -\gamma \mathbf{M} \times \mathbf{H}. \tag{1.7}$$

When there is only the external constant magnetic field **H**, the solution of equation (1.6) describes the infinite free precession of the magnetization vector around this field with the Larmor precession frequency.

With the expression (1.6) in mind let us now examine an isotropic ferromagnetic specimen with purely spin magnetism in uniform magnetic field **H** with weak homogeneous time-varying component **h** ($|\mathbf{h}(\mathrm{t})| \ll |\mathbf{H}|$), which changes harmonically with a frequency ω. Also we assume that **h** acts in the x,y-plane normal to the vector **H**

directed along z axis. If the dimensions of the specimen are small comparing with the depth of penetration of the high frequency AC field **h** (skin effect) and its wavelength in the specimen, then the field $\mathbf{h}(t)$ inside the sample can be assume homogeneous in magnitude and direction, thus its phase will be practically constant. In this case the precession of the specimen magnetization induced by the harmonic excitation field $\mathbf{h}(t)$ will also be homogeneous.

Since the field acting on the spin system consists of the high magnitude constant part **H** and low magnitude time-varying low amplitude component $\mathbf{h}(t)$ we will also separate magnetization of the system in two parts $\mathbf{M_0}$ and $\mathbf{m}(t)$, so the total magnetic moment of the sample is given by:

$$\mathbf{M} = \mathbf{M_0} + \mathbf{m}(t), \tag{1.8}$$

with the condition $|\mathbf{m}(t)| \ll M_0$. The static magnetic magnetization vector $\mathbf{M_0}$ is parallel to the magnetizing field **H.** In that case the high frequency magnetization vector $\mathbf{m}(t)$ varies harmonically and confined to the x,y-plane similar to $\mathbf{h}(t)$.

Substituting expression for magnetization (1.8) into equation (1.7), using the linearity of vector product and ignoring the term $\mathbf{m} \times \mathbf{h}$ of the second order of smallness, we obtain:

$$\frac{d\mathbf{m}}{dt} = -\gamma \mathbf{M} \times \mathbf{h} - \gamma \mathbf{m} \times \mathbf{H}. \tag{1.9}$$

After solving differential equation (1.9) for **m** we find:

$$\mathbf{m} = \chi\mathbf{h} - \mathrm{i}\,(\mathbf{G} \times \mathbf{h}), \tag{1.10}$$

where i is the imaginary unit, χ is the dynamic susceptibility and $\mathbf{G}$ is the gyration vector. Expanding these variables in greater detail:

$$\chi = \chi_0 \frac{\omega_0^2}{\omega_0^2 - \omega^2};\ \mathbf{G} = \chi_0 \frac{\gamma\omega}{\omega_0^2 - \omega^2}\mathbf{H};\ \chi_0 = \frac{\mathrm{M}}{\mathrm{H}};\ \omega_0 = \gamma\mathrm{H}. \tag{1.11}$$

It should be noted here that dynamic magnetic susceptibility χ derived in (1.11) shows Lorentzian profile with respect to the frequency of excitation field ω. Such spectral line shape is typical for a number of various systems including atoms, molecules and ions. Besides that, the first and the last expressions in (1.11) suggests that in the case when the magnitude of external applied field $\mathbf{H}$ is varied and the excitation field frequency is locked, the shape of spectroscopic profile is still described by Lorentzian profile, see Figure 1.9 below.

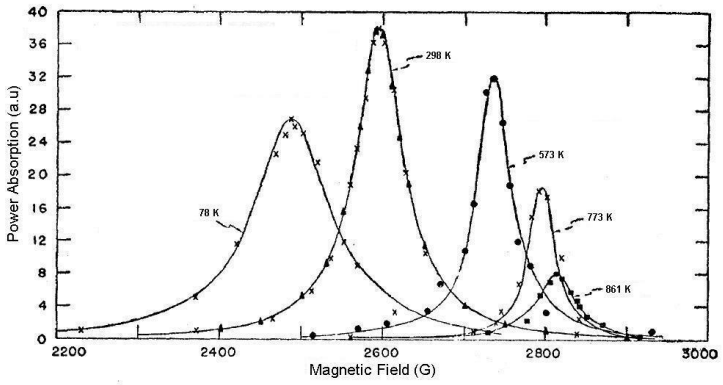

Figure 1.9 Direct resonance absorption versus dc magnetic field at 9 GHz in a sphere $NiFe_2O_4$ around Curie transition (adapted from [7]).

From (1.10) we can conclude that in crossed constant and variable magnetic fields a magneto-isotropic medium becomes gyrotropic. Using (1.9) and taking into consideration that $\mathbf{G} \parallel \mathbf{H}$ and $\mathbf{h} \equiv (h_x, h_y, 0)$, we have

$$\begin{aligned} m_x &= \chi h_x + iGh_y \\ m_y &= -iGh_x + \chi h_y \\ m_z &= 0. \end{aligned} \tag{1.12}$$

From (1.12) we can see that at small high frequency field amplitudes the magnetization vector **m** rotates in the x,y-plane at right angles to the constant field component **H.**

While the equation (1.5) allows one to calculate resonance the conditions it provides little detail regarding the evolution of magnetization of a ferromagnetic solid with time. The most widely used dynamical model for the motion of the magnetization in ferromagnetic solids was proposed by Lev Landau and Evgeny Lifshitz in 1935 [8]. This phenomenological model is represented by a continuum precession equation, where the external bias field, demagnetization field, quantum-mechanical effects and magnetocrystalline anisotropy are phenomenologically taken into account by means of the effective field. The Landau-Lifshitz equation reads in its original form:

$$\frac{\partial \mathbf{M}}{\partial t} = -\gamma \mathbf{M} \times \mathbf{H}_{\text{eff}} - \lambda \mathbf{M} \times (\mathbf{M} \times \mathbf{H}_{\text{eff}}), \tag{1.13}$$

where **M** is the vector of magnetic moment, $\mathbf{H}_{\text{eff}}$ is the vector of the effective magnetic field, γ is the gyromagnetic ratio and λ is the phenomenological damping parameter. The left hand side of the equation (1.6) contains the partial derivative with respect to time. Equation (1.6) was later modified by T. L. Gilbert and the resulting expression is now used for the most analytical applications with additional term:

$$\frac{\partial \mathbf{M}}{\partial \mathrm{t}} = -\gamma\left(\mathbf{M} \times \mathbf{H}_{\text{eff}} - \eta \mathbf{M} \times \frac{\partial \mathbf{M}}{\partial \mathrm{t}}\right). \tag{1.14}$$

Presented above is the most widely used form of Landau-Lifshitz-Gilbert equation with the damping parameter η. The damping term introduces an action analogous to a viscos force acting on precessing magnetic moment, see Figure 1.10.

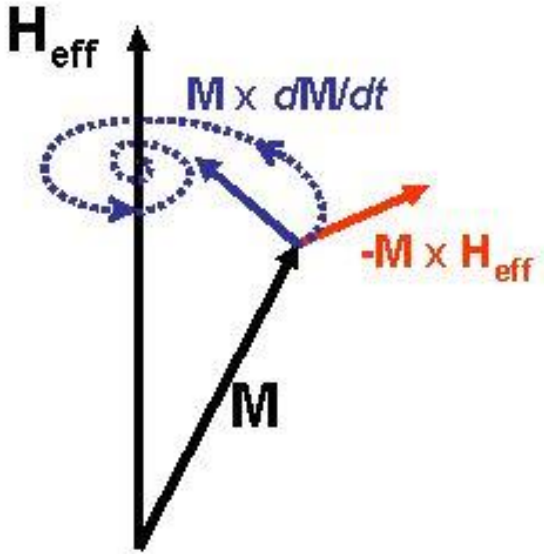

Figure 1.10 The terms of the Landau–Lifshitz–Gilbert equation: precession (red) and damping (blue). The trajectory of the magnetization (dotted line) is drawn under the simplifying assumption that the effective field $\mathbf{H}_{\text{eff}}$ is constant.

Chapter 2. Methods and Materials

2.1 Nanofabrication

The two primary nanofabrication techniques used in our studies are electron-beam lithography and lift-off. Here we will present certain details of the nanofabrication process in greater detail.

The fabrication process starts with silicon wafer with natural silicon oxide layer on top. During the first step a thin layer (about 5 nm) of Tantalum is sputtered using Ultra High Vacuum (UHV) magnetron sputtering system. This layer serves as adhesion promoter and its main role is to bind the fabricated later nanostructures to the Si substrate. Ta seed layer is important during the lift-off step where good adhesion between the substrate and fabricated nanostructures is crucial.

Deposition of Tantalum was followed by application of 210 nm thick layer of electron beam sensitive polymer Poly Methyl Methacrylate (PMMA), also called e-beam resist. PMMA is the standard positive e-beam resist and remains one of the highest resolution resists available. Application of PMMA was done using Brewer Cee 200 Spin Coater at 3000 RPM for 1 min. The amount of solvent in PMMA solution should be carefully monitored to achieve the desired film thickness. After spinning, the wafer was placed on a hotplate preheated to the temperature of 180 °C to accelerate evaporation of

the solvent and solidification of the PMMA film. PMMA film thickness was verified using Atomic Force Microscope (AFM).

During the next step PMMA resists is patterned using e-beam lithography. The basic idea behind electron beam lithography is similar to optical or any other lithographies. The substrate that is coated with a thin layer of resist, which is chemically modified during the exposure to the 50 keV electron beam, see Figure 2.1 (a), so that the solubility of exposed (non-exposed) areas can be dissolved in a specific solvent (positive (negative) lithography). This process is called development (by analogy with development of photographic films), see Fig 2.2 (b).

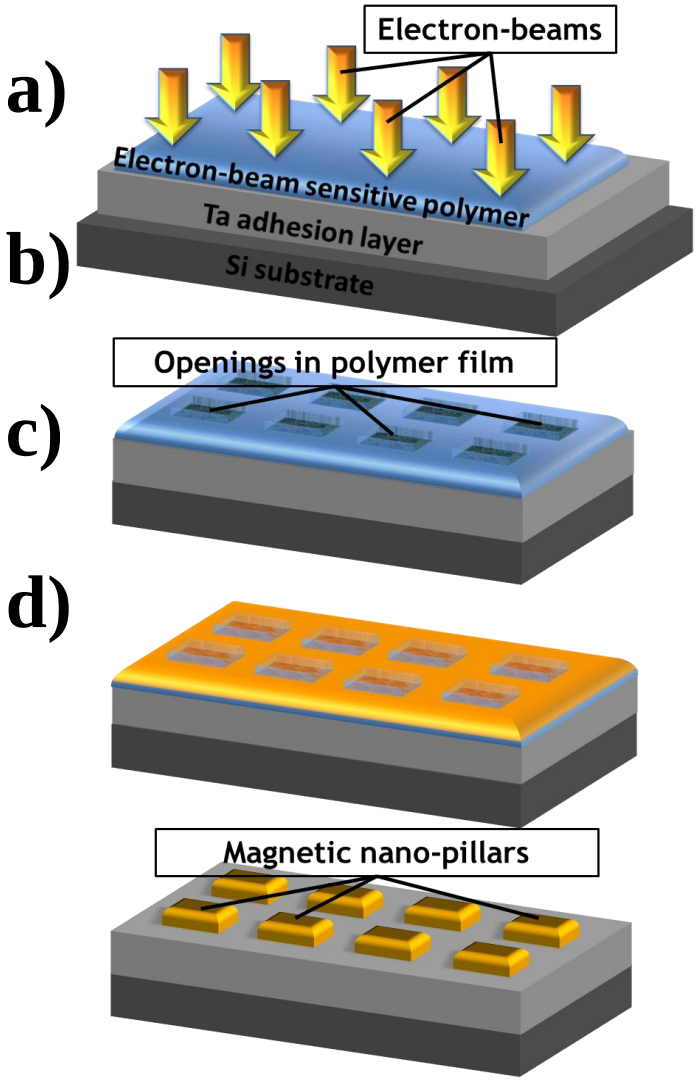

Figure 2.1 Nanofabrication process steps: (a) e-beam patterning, (b) pattern development, (c) e-beam evaporation of permalloy, (d) lift-off.

After the removal of the exposed resist (development) a 60 nm thick layer of $Ni_{80}Fe_{20}$ (permalloy) is deposited on the substrate by means of e-beam evaporation. E-beam evaporation provides uniform well-directed deposition with minimal anount of material of the sidewalls of the nanostructures. On the areas exposed to the electron beam the deposited metal sticks to the adhesion layer supported by substrate, while on the unexposed areas the metal sticks to the resist surface (Figure 2.1 (c)).

During the last fabrication step, the lift-off, the sample is placed in ultrasonic bath with acetone. After this step the resist is dissolved in the solvent (lift off). The permalloy

sticking to the resist is removed and only the metal sticking to the Ta seed layer remains, Figure 2.1 (d).

2.2 Ferromagnetic Resonance Spectroscopy Setup

FMR spectrometer is a tool to measure electromagnetic (EM) wave absorbed by a sample of interest under the influence of external DC or modulated DC magnetic field. In principle, the spectrometer should consist of a radio frequency excitation source, microwave detector, and transmission line which connects sample and EM source. The precession frequency of ferromagnetics typically lies in microwave ranged of the spectrum from 0.1 GHz to about 100 GHz, therefore, FMR absorption occurs at microwave range. The generation, detection and transmission at such this high frequency are not as simple as those for DC or low frequency electronics. According to transmission line and network theories, impedance of 50 Ω between transmission line and load has to be matched for optimization of energy transmission. Figure 2.2 is the schematic of view of FMR spectrometer with all its components design used in our experiments. In addition to standard FMR setup, our system allows to adjust the direction of the external bias magnetic field relative to the plane of the sample. The dashed line on the Figure 2.2 shows the axis of rotation.

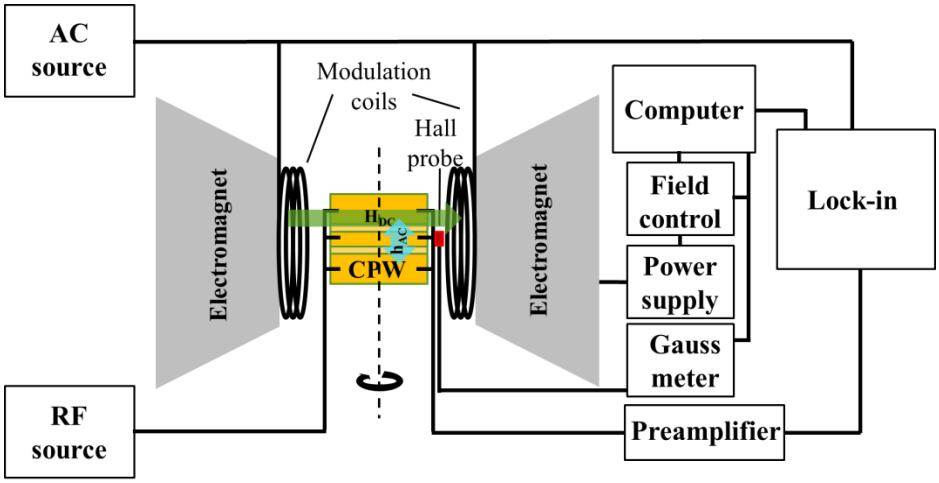

Figure 2.2 Experimental setup for microwave spectroscopy.

Figure 2.3 shows the configuration of the high frequency AC field produced by the coplanar waveguide used in our experimental setup. High frequency field is used to excite resonant precession of magnetization in the sample.

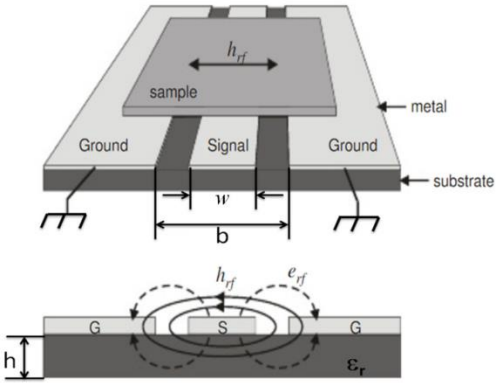

Figure 2.3 AC field and sample configuration in FMR spectrometer, image is the courtesy of intechopen.com.

2.3 FMR Measurement Scheme

In field sweep modulated measurement scheme there is a small field H_a, with modulation frequency of ω superposing on top of external DC magnetic field, H_0:

$$H(t) = H_0 + H_a \cos(\omega t), H_a \ll H_0, \tag{2.1}$$

where ω is the frequency of modulating field produced by modulating coils, see Figure 2.2, and t is time.

Expanding measured signal is V_{FMR} that is a function of applied field H in a Taylor series at the field H_0 we have

$$V_{FMR}(H) = V_{FMR}(H_0) + \left.\frac{dV_{FMR}}{dH}\right|_{H=H_0} H_a \cos(\omega t) + \ \ldots \tag{2.2}$$

There is also another signal, the reference signal, internally generated by the lock-in amplifier, which has the same frequency as that of the modulation field, but with a phase shift φ:

$$V_{ref} = V_0 \cos(\omega t + \varphi), \tag{2.3}$$

where V_0 is the amplitude of the reference signal.

In the experimental setup the multiplication of the signals (2.2) and (2.3) is performed by the lock-in amplifier. After multiplication and trigonometric simplifications we have the following expression for the product of two signals:

$$V_{FMR}(H) \times V_{ref} = V_{FMR}(H_0)V_0\cos(\omega t + \varphi) + \frac{1}{2}\frac{dV_{FMR}}{dH}\Big|_{H=H_0} H_a V_0\cos(\varphi) + \frac{1}{2}\frac{dV_{FMR}}{dH}\Big|_{H=H_0} H_a V_0\cos(2\omega t + \varphi) + \cdots \quad (2.4)$$

The first and third terms in equation (2.4) can filtered out by using a low pass filter with cutoff frequency setting at $\omega/2$ or lower. The second term is time independent, proportional to derivative of the input signal and magnified by H_a, which has a maximum if the phase, φ, is locked to 0.

Modulated field sweep FMR spectroscopy provides viable approach to study magnetization dynamics in both continuous and nanopatterned films. It is effective in improving SNR of the test system and, at the same time, relatively easy to implement.

Chapter 3. Effects of Lattice Geometry on Ferromagnetic Resonance Spectrum

3.1 Motivation

In this paragraph we consider the effects of the geometry of various lattices as well as magnitude and direction of external magnetic field on variety of magnetic textures and resonance modes observed in the arrays of dipolarly coupled nanopillars. Observed experimental result supplemented with micromagnetic simulations for better visualization and understanding of the phenomena.

In conventional granular magnetic recording media the grains of material are effectively exchange decoupled due to intentionally grown layers of oxide at the grain boundaries. Although in longitudinal and perpendicular magnetic recording media dipolar stray fields present in the system they are significantly lower than contribution of the shape or magnetocrystalline anisotropy of the material. Contrary, in so called magnonic crystals the situation is quite different. Here dipolar interaction plays a crucial role defining the properties of magnetic metamaterial.

In broader view, technological requirements to increase operation frequency and areal density of magnetic random-access memory (MRAM), magnetic logic and magnetic data storage devices will eventually cause the effects of collective magnetodynamic behavior at microwave frequencies to play significant role in these systems. Microwave part of the spectrum is of special interest because it represents the timescales characteristic for read and write processes in HDD and MRAM. To gain insight into the role of the long range dipolar interaction we performed a study of magnetization dynamics in millimeter-sized arrays of closely packed dipole coupled rectangular

nanomagnets of relatively high aspect ratio $\varepsilon = 0.6$. Most of the previous studies were concentrated on the systems where one of the dimensions is significantly reduced. For example large amount of attention was turned to nanodisks with the radius much larger than the height of a disk ($\varepsilon \ll 1$) or magnetic nanowires. In these cases shape anisotropy plays the dominant role in magnetic behavior of the system and effects of interdot interactions are negligible. Here we consider rectangular nanopillars with dimensions $100 \times 100 \times 60$ nm. With such choice of geometry, these systems have the potential to show significant influence of the dipole interaction on the FMR spectrum.

3.2 Sample Preparation and Measurements

For our experiments we prepared three two-dimensional arrays of isolated $Ni_{80}Fe_{20}$ (permalloy) rectangular magnetic nanodots by means of e-beam lithography and lift-off technique. In presented report the dimensions of the rectangular nanodots were kept constant ($100 \times 100 \times 60$ nm) and the lattice parameters of the arrays were varied. We kept the ratio of the edge-to-edge distance to the center-to-center distance the same and about 1.6 in all three arrays to isolate the effects pertaining to interdot interactions from the effects of the geometry of individual nanomagnets (demagnetizing field). Only the arrangement of the nanomagnets in arrays was varied. In this study square, centered square and hexagonal lattices were tested. In our experiments the nanomagnets had the side length of 100 nm and 60 nm height.

To probe the magnetic states in nanomagnets, magnetostatic properties of the arrays were characterized using Alternating Gradient Force Magnetometer. In this study resonance spectra were obtained using modulated field-sweep FMR spectrometer with

variable angle of the bias field. The ferromagnetic resonance in the system was excited by AC magnetic field with the frequency 9.8 GHz generated by coplanar waveguide.

After fabrication samples the quality of the samples was characterized with Scanning Electron Microscope to validate the geometry and positions of nanodots , see Figure 3.1.

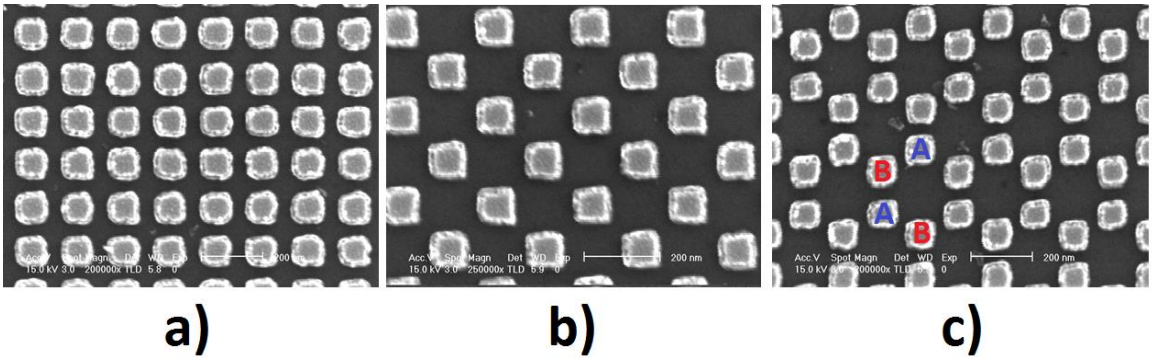

Figure 3.1 SEM images of 100nm x 100nm x 60nm nanodots arranged in (a) square lattice; (b) triangular lattice; (c) hexagonal lattice.

In the structures shown on the Figure 3.1, the interdot spacing was chosen such that the ratio of the edge-to-edge distance to the center-to-center distance is the same for all three samples and equal ~0.67. Colored letters “A” and “B” show nanomagnets that comprise the two distinct sublattices in hexagonal array.

Analyzing the shapes of the nanomagnetis on the Figure 3.1 one can notice that corners of the nanomagnets are the “sharpest” on the image (b) – centered square lattice and that the shape of nanomagnets on the image (c) deviate from the ideal square form. This is likely due to the proximity effect observed in e-beam patterned arrays. It can be explained by the non-uniformity of actually deposited dose during the e-bam printing process.

3.3 Magnetostatic Measurements

Some aspects of magnetic properties of a system can be gained from the magnetostatic measurements. For that we performed characterization using Alternating Gradient Field Magnetometer (AGFM) which provides the net magnetization of the system as a function of the strength of externally applied magnetic field, see Figure 3.2 below. For each of the samples we ran in-plane and out-of-plane measurements.

In AGFM device the magnetic sample is mounted on the end of a cantilevered rod that is attached to a piezoelectric element. The sample is magnetized by a DC field (variable in magnitude), and is simultaneously subjected to a small alternating field gradient produced by additional magnetic coils. The alternating field gradient exerts an alternating force on the sample, proportional to the magnitude of the field gradient and to the magnetic moment of the sample. The resulting deflection of the cantilever rod is measured by the voltage output of the piezoelectric element. By operating at or near a mechanical resonance frequency of the cantilever, the output signal is greatly amplified. For most of the samples we masured, the operating frequency is in the range of 400 – 900 Hz, with mechanical quality factor Q values of 300 – 500.

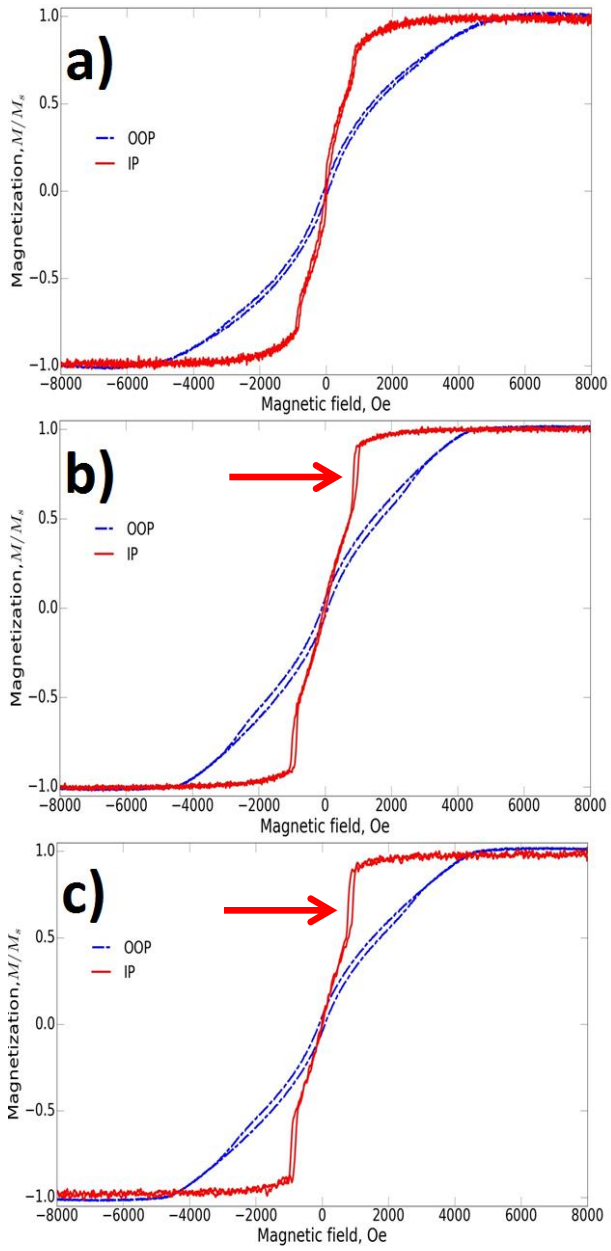

Figure 3.2 Characterization of magnetic anisotropy in arrays of closely packed rectangular nanomagnets using AGFM.

On the firuew 3.2, the magnetization normalized to the saturation magnetization of each of the samples. Out-of-plane (blue dashed line) and in-plane (continuous red line)

hysteresis loops measured: (a) sample with square lattice, (b) cantered square lattice and (c) hexagonal lattice.

From the magnetization hysteresis loops it can be seen that all three samples saturate at lower magnetic fields when the external bias field is parallel to the plane of a sample. This behavior indicates the in-plane anisotropy and possible presence of the inter-dot magnetostatic coupling. Since the aspect ratio (height / width, $\varepsilon = 0.6$) of individual nanonmagnets implies the in-plane shape anisotropy of each of the nanomagnets, it is impossible to deduce the role of interdot dipolar coupling without doubt.

3.4 Magnetic Vortices

Yet centered square and hexagonal lattice samples, Figure 3.2 (b) and 3.2 (c), marked with red arrows, show features characteristic for magnetic vortices. Vortex states are some of so called topological defects and are very stable formations in magnetic systems. Other topological defects observed in magnetic systems include domain walls and skyrmions. Figure 3.3 shows example of evolution of magnetic texture in a cylindrical nanomagnet at different states of magnetic vortex nucleation and annihilation process. In these calculations magnetic field applied transversely to the axis of the cylinder (in-plane).

Returning to our results, absence of the vortex states in the sample with the square lattice arrangement, sample (a), provides additional evidence of dipolar interdot coupling as the geometry of individual nanomagnets is the same for all the samples and cannot explain differences in observed hysteresis loops alone. Based on our experimental results

we can conclude that the ground state of arrays of interacting nanomagnets can be controlled through the geometry of the lattice alone and there is possibility of relation between the topology of the lattice and topology of magnetic texture inside the magnetic nanodots.

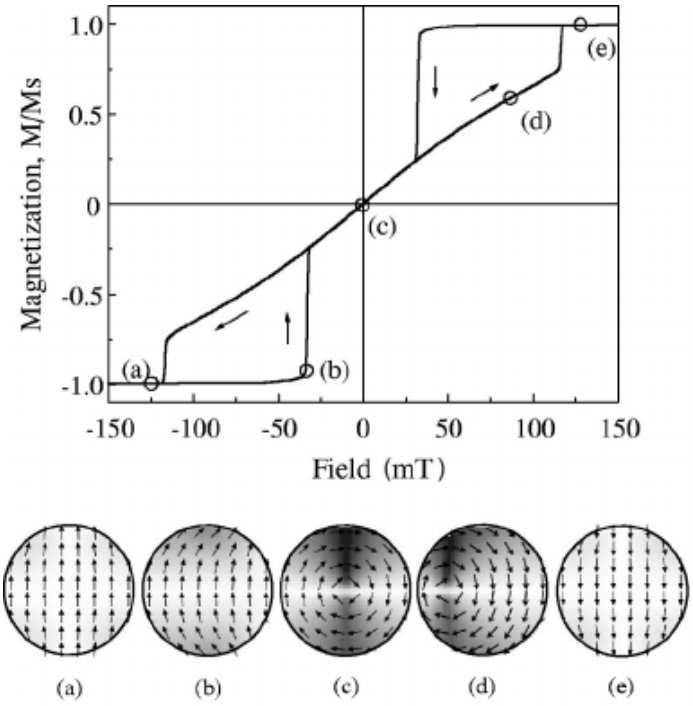

Figure 3.3 The typical hysteresis loop and magnetization reversal process due to the vortex nucleation, displacement, and annihilation as calculated with micromagnetic solver for a dot with radius 0.1 um and height 30 nm.

Presented on the Figure 3.2 structure characterized by the low aspect ratio $\varepsilon = 0.6$. In this case the "footprint" of magnetic vortex is more pronounced – the openings of the loop are considerably wider comparing to that of nanostructures with relatively high aspect ratio such as in our samples [9].

3.5 Magnetization Dynamics in Arrays of Coupled Nanodots

In this section we study the evolution of the FMR spectrum of arrays of magnetic nanodots arranged in three different lattices with respect to the direction of externally applied bias field. Depending on the orientation of the magnetization induced by the applied field, the direction of the stray field produced by the neighboring nanomagnets onto each other changes from parallel to antiparallel to the magnetization of the nanomagnets. Basic model with just two interacting magnetic dipoles provide a simple qualitative picture of the phenomena, see Figure 3.4.

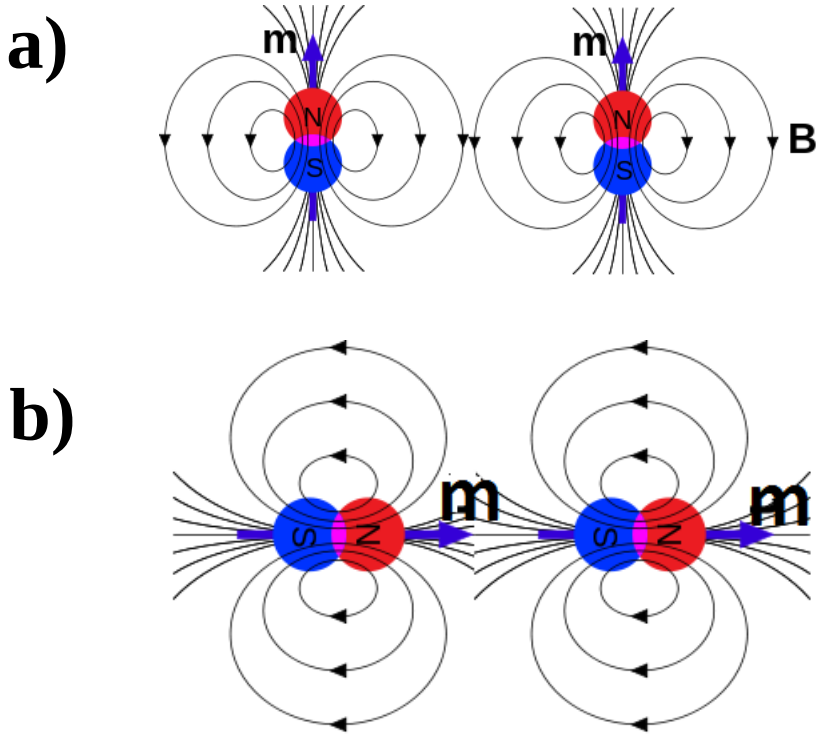

Figure 3.4 Parallel and antiparallel configuration for two interacting magnetic dipoles. Black lines and arrows show direction of stray magnetic field. Blue arrows show magnetic moment vectors.

When magnetization vectors are parallel to each other and perpendicular to the line connecting them, as shown on the Figure 3.4 (a), the stray field from the neighboring dipoles is antiparallel to their magnetization vectors. This is a high energy state. In case when two magnetization vectors of the magnetic dipoles are collinear, Figure 3.4 (b), the stray field produced by each dipole at the location of the neighbor is parallel to magnetization direction of both dipoles. This state corresponds to the minima of energy of this simple system. Of course, in the real system these interactions are more complicated especially when there is more than one neighbor involved in interaction.

Here we consider the three arrays, Figure 3.1 (a), (b) and (c), as the systems of interacting nanodots that are forming a media with unique metamaterial properties. These artificial materials can host excitations of magnetic order – spin waves that are of major interest in magnonics. As we show later in this chapter, one way to control the properties of such media can be achieved by means of adjusting the lattice geometry.

We start the study of magnetodinamic behavior of arrays of nanomagnets by comparing the FMR spectra of continuous film to that of arrays of rectangular nanomagnets with dimensions $400 \times 400 \times 60$ nm (width × length × height), see Figure 3.5. This sample was fabricated using the same process as the samples shown on the Figure 3.1 (a), (b) and (c). Typically, three distinct regions in the FMR spectra are observed for the nanomagnet array of 400nm wide squares, 60nm thick and 67% duty cycle (Figure 3.5, inset (a)). In the first region, when the magnetic field angle varies from 0 degrees until the first critical angle θ_1^c, a single dominant resonance peak is observed which is similar to a continuous permalloy film of identical thickness.

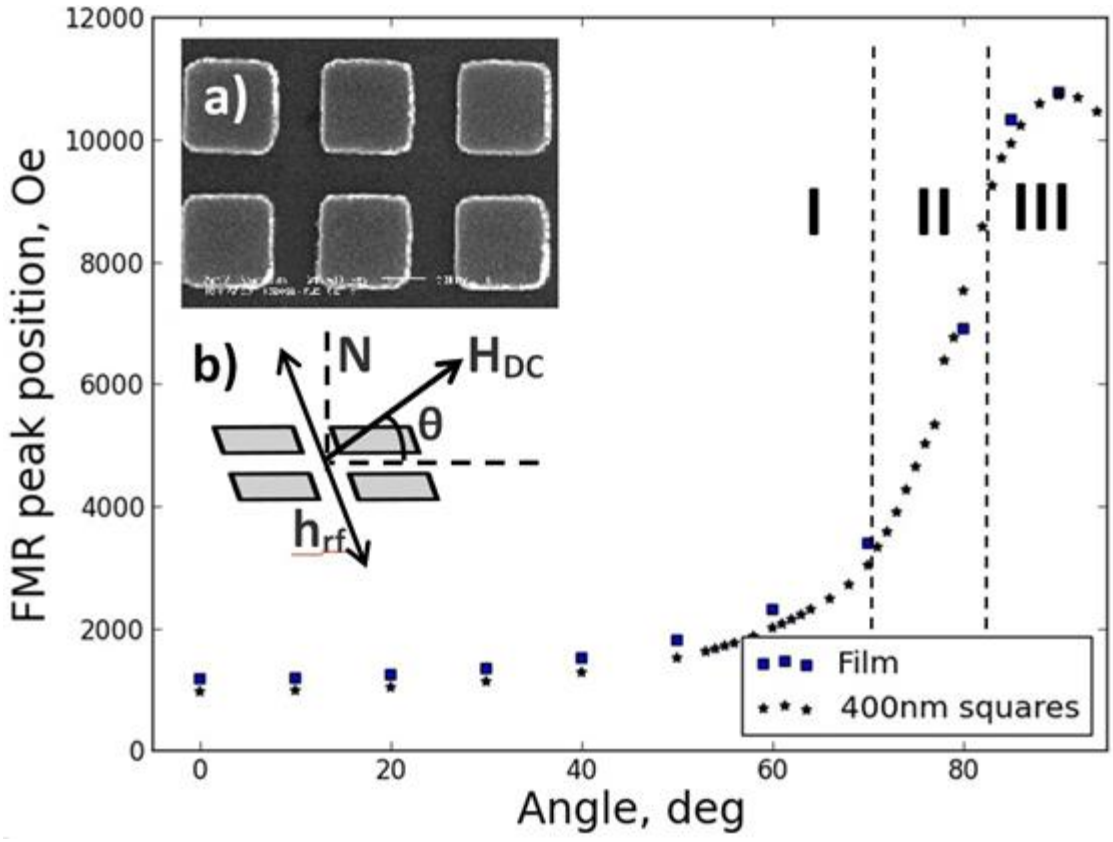

Figure 3.5 The main peak position changes as the applied magnetic field is varied from parallel with the sample's plane towards normal to the sample's plane.

The nanomagnets shown on the Figure 3.5 is 400nm wide, 60nm thick with a duty cycle of 67%. Inset (a) is the top-down SEM image of the sample; inset (b) is a schematic of the measurement, where N is normal to the plane of the sample, H_{DC} is the magnetic field, h_{rf} is the magnetic component of the microwave driving resonant precession. Within region I, only one FMR peak is observed; region II demonstrates clear multimode SW resonance; and in region III, a single peak observed.

In the second region, where the angle θ is varied in the range of $\theta_1^c < \theta < \theta_2^c$, multiple resonance peaks are observed. Finally, within the range $\theta_2^c < \theta < 90°$ the multimode spectrum reduces to a single dominant peak, see figure 3.6. The general

profile of the resonance peak position vs. direction of the bias field is similar to the case of the continuous permalloy film with one major difference. It is important to note that in continuous film only one resonance peak observed. Thus boundary conditions play important role in magnetodynamic spectra even of fairly large magnetic structures.

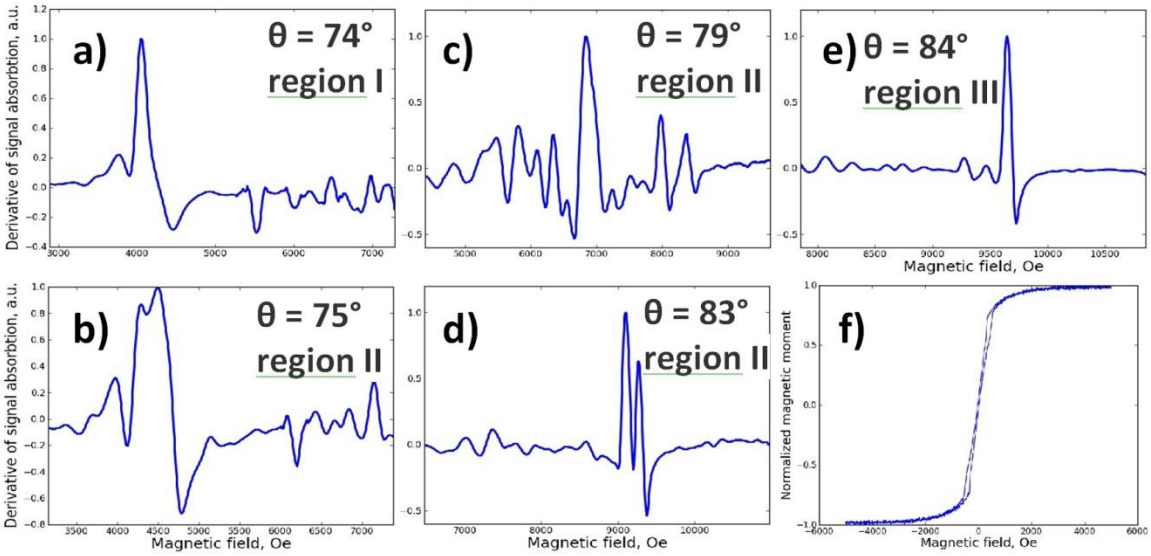

Figure 3.6 Selected FMR peak profiles are shown for each region. A single dominant peak is observed until (a) θ = 74°. At (b) θ = 75°, the new peaks begin to appear until the maximum number peaks are observed at (c) θ= 79°.

On the figure 3.6, the number of peaks decrease as seen in (d) θ = 83° until there is reduced to only one dominant peak at the value (e) θ = 84°. Segment (f) is the normalized hysteresis loop of the patterned sample obtained at external field applied in-plane to the array.

From the Figures 3.5 and 3.6 it can be seen that FMR spectrum of nanopattened films is quite non-trivial. To better assess the details of evolution of FMR spectrum of the samples with various lattices we performed measurements with the step $\theta = 1°$ in the

range from $\theta = 0°$ (in-plane) to $\theta = 100°$ recording the entire spectrum to capture all the accessible resonance modes.

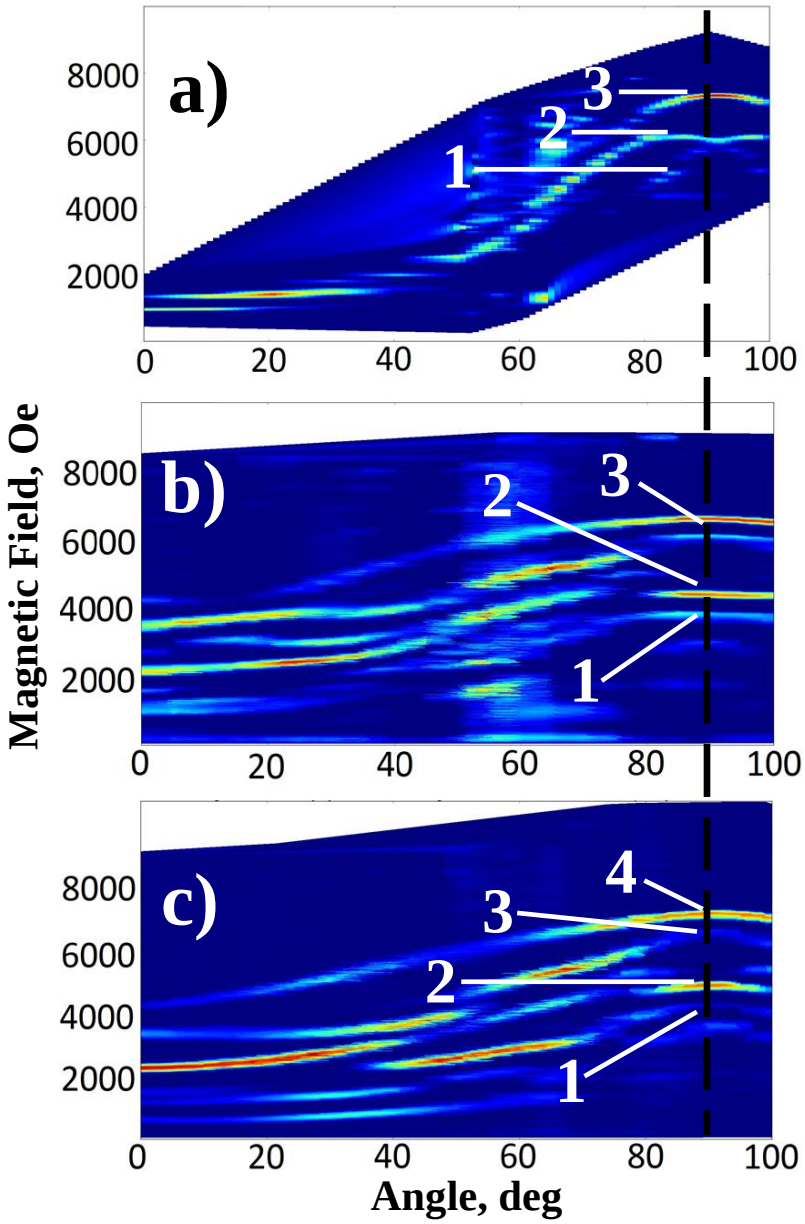

Figure 3.7 Evolution of FMR spectra with respect to direction of the external bias field of (a) square lattice, (b) centered square lattice and (c) hexagonal lattice.

Vertical black dashed line on the Figure 3.7 shows the “slice” of the spectrum at 90° (out-of-plane) external field. Numbers indicate the observed distinct modes. Color shows the relative peak amplitude with red being the highest and blue – lowest amplitude.

There are several differences comparing the spectra shown on the Figures 3.5, 3.6 and 3.7. First, the resonance mode splitting at high angles (near out-of-plane) observed in the samples with 100 nm side length, Figure 3.7, is absent or significantly suppressed in the array of larger nanomagnets with side length of 400nm. This result is in agreement with the theoretical predictions that suggest that distance between the neighbor resonance peaks of standing spin waves in a perpendicularly magnetized circular dot is inversely proportional to the dot radius.

Another important difference is the absence of so called edge modes observed at low grazing angles (near in-plane magnetization). These modes cannot be seen in the samples with 400 nm side length, Figure 3.5 and Figure 3.6 and in the square lattice with 100 nm nanomagnets, compare Figure 3.7 (a) with Figure 3.7 (b) and (c).

Chapter 4. Ferromagnetic Resonance Mode Structure in Arrays of Magnetostatically Coupled Nanopillars

4.1 Motivation

Here we present a study of the effects of the dipolar coupling on the magnetic texture and ferromagnetic resonance (FMR) spectra in arrays of closely packed interacting cubic permalloy nanomagnets. Our study carried out by means of the modulated field sweep FMR spectroscopy with the DC bias magnetic field applied in the range of angles from in-plane to out-of-plane to the 2D arrays of cubic nanomagnets with 60nm side length. From the evolution of the FMR spectrum with respect to the angle of applied bias field we observe that FMR peak splitting and multiple resonance modes generation is affected by the nanomagnet's geometry, intermagnet distance and magnetic field orientation relative to the plane of a sample. In particular, two types of resonance modes (shape and lattice) are well pronounced in the experimental FMR spectra and affected by geometrical parameters of the arrays. Further, we show analytically that these modes can be characterized by effective demagnetizing factors representing different symmetries of the system. Our experimental observations supplemented by the micromagnetic simulations to elucidate the origins of the observed ferromagnetic resonance spectra. From the micromagnetic simulations we conclude that magnetic

texture in the cubic nanomagnets is modulated by the stray field produced by neighboring nanomagnets and is likely to influence the FMR spectrum in closely packed interacting magnetic nanocubes.

4.2 Overview

With intensification of the search for faster and more energy efficient alternatives to conventional electronics-based computation architectures and data storage systems, considerable attention was turned to the areas of spintronics and magnonics [10]-[14]. These areas of research and technology deal with the collective excitations of magnetic order in thin films, nanopatterns and in macroscopic scale bodies. In recent years topic of reprogrammable magnetic systems has gained the ground as well [15], [16]. For potential data storage applications, magnetization dynamics in RF magnetic field plays crucial role in microwave assisted magnetic reversal. In broader view, technological requirements to increase operation frequency and areal density of magnetic random-access memory (MRAM) and magnetic data storage devices will eventually cause the effects of collective magnetodynamic behavior at microwave frequencies to play significant role in these systems. Good understanding and ability to tune and control the magnetic properties of nanostructured materials will play the key role in the success of development and optimization of the new computation architectures and data storage systems [17], [18].

Significant progress has been made in theoretical and experimental studies of spin wave generation and propagation in arrays of antidotes and magnetization dynamics in nanomagnets and magnonic crystals [19] - [23]. Considerable research effort has been

focused on the magnetization dynamics in arrays of nanomagnets with weak interdot coupling or no interaction at all. Several interesting phenomena such as edge modes, spin wave quantization and confinement were studied theoretically [24] - [26] and characterized experimentally in such systems [18], [27] - [31]. Also, previous studies indicate considerable influence of the lattice symmetry on the magnonic band structure of closely packed ferromagnetic nanodots magnetized in-plane at various azimuthal angles [32], [33]. Large progress has been made in development of theoretical formalism for magnetic excitations in arrays of dipolarly coupled macrospins [34]. Dependence of the FMR spectrum and magnetization of arrays of isolated nanomagnets on the angle of applied external field was studied for nanoellipses with relatively low aspect ratio [35]. Yet understanding of the details and role of the interdot magnetostatic interaction in the collective dynamic behavior and magnetic texture of magnetic nanoarrays still has considerable gaps. As to our knowledge, there are no reports of magnetization dynamics in arrays of sub-100nm magnetostatically coupled nanodots with respect to polar angle of externally applied DC bias magnetic field, which is causing the non-zero out of plane magnetization component. Arrays of nanomagnets with relatively high aspect ratio (height/side length) $\xi = h / l = 1$ to 0.5 and small intermagnet spacing are well suited for this study as magnetodynamic phenomena in such bodies is not entirely dominated by the shape anisotropy or by the confinement due to the boundaries of individual nanomagnets. In this case, significant contribution of the magnetostatic coupling to the behavior of the dynamic system can be expected.

As the orientation of the DC bias magnetic field and magnetization of individual nanomagnets in a 2D square array continuously varied from the in-plane to out-of-plane,

the type of dipolar coupling between certain neighboring nanomagnets changed from ferromagnetic (FM) to antiferromagnetic (AFM) or vice versa depending on the relative position of nanomagnets in the lattice. Such changes of the type of the dipole coupling in magnetostatically interacting system are predicted to cause splitting of the resonance modes [22]. The difference in the magnetization dynamics of the in-plane and out-of-plane magnetized arrays is well observed and analyzed therefore it is of high interest to fill in the gap and characterize the full evolution of the spin wave spectra as the magnetization angle gradually varied from the in-plane to out-of-plane to a 2D array of interacting nonamagnets.

Study of collective excitations in magnetic nanosystems presents large number of challenges due to variety of the factors that contribute to the richness of the phenomena: exchange interaction within the nanomagnet, magnetocrystalline anisotropy, shape anisotropy, long-range dipole coupling and the effects of the surface anisotropy and roughness. Depending on the size of the nanomagnets, their shape, composition and geometrical parameters of the array, various factors influencing magnetization dynamics can be brought to dominance thus allowing the control and tenability of the magnetodynamic properties of magnetic meta-material.

To gain insight into the role of the long range dipolar interaction we performed a study of magnetization dynamics in millimeter-sized arrays of closely packed dipole coupled cubic nanomagnets of relatively high aspect ratio $\varepsilon = 1$ to 0.5. With such choice of geometry, these systems have the potential to show significant influence of the dipole interaction on the FMR spectrum. The arrays in our study were magnetized at various angles to the plane of the samples to induce various types (FM or AFM) of inter-dot

interactions. The FMR spectrum was obtained at various angles of magnetization relative to the plane of the sample.

4.3 Experimental Methods and Procedures

For our experiments we prepared three two-dimensional arrays of isolated $Ni_{80}Fe_{20}$ (permalloy) cubic magnetic nanodots using the lift-off technique. In presentedreport the dimensions of the nanodots were kept constant and the lattice parameters of nanoarrays were varied. In our experiments all cubic nanomagnets had 60 nm side length and the pitch of the square array was varied from 90 nm to 180 nm.

All samples in our study were fabricated on a silicon substrate with a thin layer of natural oxide. Prior the nanostructure fabrication, a thin seed layer of Ta (5 nm) was deposited using UHV magnetron sputtering to promote the adhesion of permalloy to the substrate. Following that, the 210nm thick layer of PMMA e-beam resist was spun and 1mm x 1mm arrays of rectangular regions were exposed to 50kV electron beam using JEOL JBX-5500FS e-beam writer. After e-beam patterning and development in IPA:Water solution (2:1), electron beam evaporation of 60nm permalloy at the constant rate of 0.2 A˚ /s at the base pressure 2 × 10−7 Torr was performed to fabricate magnetic nanostructures. The sample fabrication was finalized by the ultrasonic-assisted lift-off in acetone bath at 35C temperature. To avoid sample degradation and damage during handling and magnetic measurements, 100nm thick layer of PMMA was spun over the samples surface after scanning electron microscope (SEM) imaging.

After preparation, samples were characterized using Alternating Gradient Force Magnetometer (AGFM) to obtain hysteresis loops and information about magnetic

anisotropy of the nanoarrays. Magnetodynamic measurements were performed using field-sweep FMR spectrometer with varied orientation of DC magnetic bias field. In presented herein FMR results the 9.8 GHz AC magnetic field was generated by the coplanar waveguide antenna. Prior to magnetic measurements, the geometrical parameters of the nanomagnets were characterized with Atomic Force Microscope (AFM) and SEM to verify the dimensions and pattern quality.

Micromagnetic modeling was performed using the LLG Micromagnetics Simulator [36].

4.4 Experimental Results

All three samples in our study show the in-plane (IP) anisotropy with the coercivity H_c ranging from 6.8 to 134.1 Oe when the bias field applied IP and parallel to the sides of cubic nanomagnets, and H_c ranging from 69.7 to 134.1 Oe for the out-of-plane (OOP) measurements. The IP and OOP hysteresis loops of the arrays shown on the Figure 4.1 along with the top-down SEM images of the arrays with various duty cycles (ratio of the side length of nanomagnet to the pitch of pattern). Arrays magnetized IP reach the saturation at lower externally applied fields comparing to the magnetization loops obtained in OOP measurements for the same samples, Figure 4.1 (a), (b) and (c). Squareness (M_s/M_r, M_r is the remanence and M_s is the saturation magnetization) and the slope of M-H curves of the samples with the duty cycles 0.67 and 0.5 is decreasing from former to later, indicating the decrease of the inter-dot coupling and IP anisotropy. In the case of the sample with duty cycle 0.33, the drastic decrease of H_c and closing of the M-

H loops at low bias field indicate that magnetization reversal is predominantly governed by the creation and annihilation of magnetic vortices.

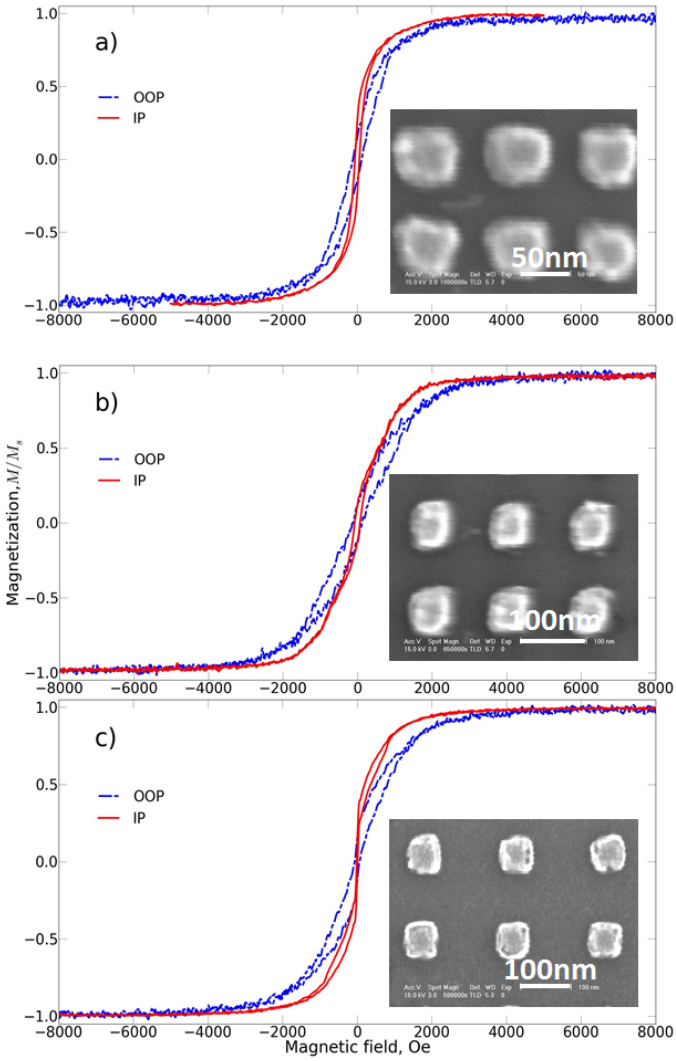

Figure 4.1 Characterization of magnetic anisotropy in arrays of closely packed rectangular nanomagnets.

On the figure 4.1, out-of-plane (blue dashed line) and in-plane (continuous red line) hysteresis loops measured using AGFM: a) sample with duty cycle 0.67, b) 0.5 and c) 0.33. All three samples saturate at lower magnetic field when the bias field is parallel to the plane of a sample. This behavior indicates the in-plane anisotropy and presence of the inter-dot magnetostatic coupling. The insets at the bottom right corners are the top-

down SEM images of corresponding arrays. The shape of the most densely packed arrays such as the one presented on the Figure 4.1 (a) is affected by the artefacts of e-beam lithography and lift-off imperfections the most due to the proximity effect. Shape of the most densely packed nanomagnets deviates from the nominally cubic shape the most.

FMR spectra obtained at various angles of the DC bias field shows rich magnetodynamic behavior in arrays of coupled nanodots. Identifying only the peaks with the highest amplitude does not reflect the whole variety of the phenomena, thus we present the FMR spectra measured in wide range of angles and DC bias field, see Figure 2 (a), (b) and c). To compose the Figure 4.2, DC bias field was applied at an angle θ^{H} to the normal of the plane of the sample and swept in the range from 0.5 to 12 kOe. Projection of the bias field on the plane of a sample was set parallel to the major axes of the square arrays. For each DC field orientation, obtained FMR spectrum was normalized to the peak with the highest amplitude. After that the 2D image was composed. This scheme of data presentation was chosen to show the relative FMR peak amplitudes and to maintain the visibility of all resonance modes on the same plot. Otherwise, presence of high intensity dominant mode at certain angles would render the lower amplitude modes difficult to see on the same graph.

The FMR spectrum of the most densely packed array has two distinct resonance modes, see Figure 4.2(a). These modes are distinguishable by their characteristic dependence on the orientation of the bias field. In this manuscript we will term the mode that shows strong dependence on the orientation of the bias field the lattice mode. The lattice mode has a well pronounced peak at $\theta^{H} = 0$, and resembles magnetodynamic behavior of a continuous film. We will call the mode with weak dependence on θ^{H} the

shape mode. Relative intensity of the resonance peaks gradually switches between the modes as the magnetization direction varied from OOP to IP. Amplitude of the shape mode, that is highest at low θ^H, gradually vanishes until it becomes almost unnoticeable when the array is magnetized IP, Figure 4.2 (a).

As can be seen on the Figure 4.2, FMR spectrum structure of the arrays of coupled nanopagnets strongly depends on the parameters of the lattice. Arrays of nanomagnets with duty cycles of 0.5 and 0.33, Figure 4.2 (b) and (c) respectively, demonstrate both similarities and differences comparing to the FMR spectra of the most dense nanopattern, Figure 4.2 (a).

Observation of non-trivial FMR spectrum allows us to conjecture that arrays of even sub-100 nm magnets demonstrate behavior that strongly deviates from a simple model of lattice with macrospins. Internal magnetic texture and dynamics is far from uniform magnetization and precession. Highly non-uniform stray fields produced by the neighboring nanomagnets play crucial role in magnetodynamic phenomena and define modal structure of the FMR spectrum.

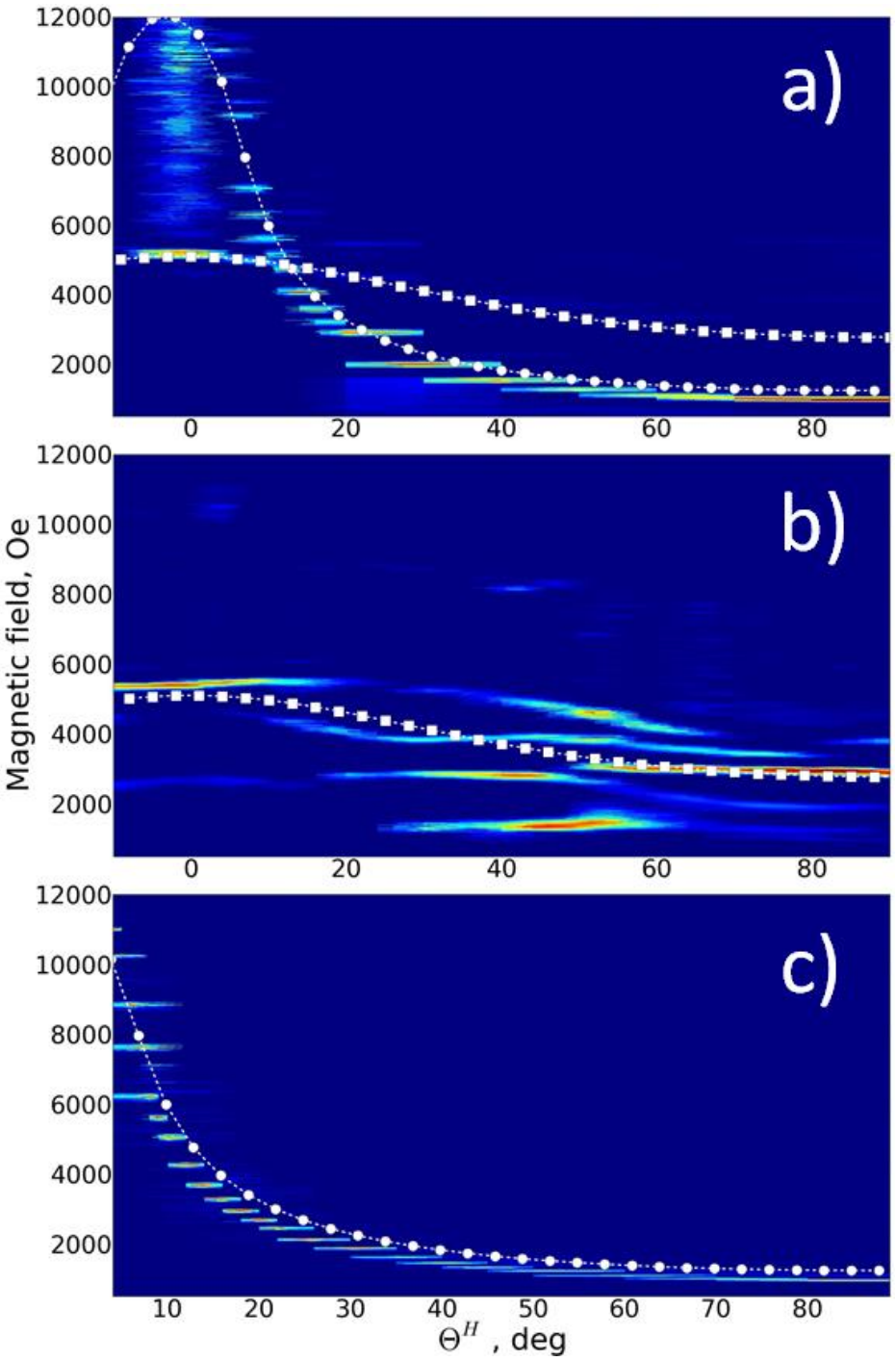

Figure 4.2 Angle dependent FMR spectra at 9.8GHz for 60nm permalloy cubes arranged in square lattice with duty cycles of: a) 0.67, b) 0.5 and c) 0.33.

On the Figure 4.2, shades of gray or red color intensity represent the resonance peak amplitude. Angle is the polar angle θ^H of the DC bias field. Rectangular and

circular markers show the theoretical values of the resonance field for the two distinct FMR modes calculated for $N^{eff} = \frac{19\pi}{18}$ and $N^{eff} = 0$ respectively. Theoretical values are not the actual fit to the experimental data and presented for qualitative comparison.

While the FMR spectrum structure of the sample with duty cycle 0.5, 2 b), is very non-trivial, unlike the sample with duty cycle 0.67, it shows absence of the lattice mode. This is in contrast to the sample with duty cycle 0.33, which has well pronounced lattice mode and the shape mode is not observed. Complicated structure of the FMR spectrum of the sample with duty cycle 0.33 is possibly due to hybridization of the resonance modes [37]. Absence of the lattice mode in the FMR spectra of the array with duty cycle 0.5 is yet to be explained. It is possibly due to the lattice mode band structure defined by the geometrical parameters of the array.

4.5 Analytic Model

To analyze the contribution of the dipole interdot interaction to FMR spectrum we start with the general expression for the free energy density of the array of uniformly magnetized rectangular prisms:

$$F = -\left(\overrightarrow{M_s} \cdot \vec{H}\right) + \frac{1}{2}\left(N_x M_{sx}^2 + N_y M_{sy}^2 + N_z M_{sz}^2\right), \tag{4.1}$$

where the first term is the Zeeman energy and the second term is the demagnetization energy. $\overrightarrow{M_s}$, M_{sx}, M_{sy} and M_{sz} are the vector of saturation magnetization at equilibrium and its components along x, y and z axes, $\vec{H}$ – applied magnetic field. N_x, N_y, N_z are the

effective demagnetizing factors of the array of nanomagnets connected by the relationship: $N_x + N_x + N_x = 4\pi$. For our case of a square lattice with rectangular nanopillars we will use simplifying condition for the demagnetization factors and assume that $N_x = N_y = N^{eff}$. Low values of N^{eff} correspond to the patterns with low aspect ratio and/or strong interdot magnetostatic coupling, thus, high IP anisotropy. In our considerations we will neglect the magnetocrystalline and surface anisotropies of permalloy.

The equilibrium orientation of the vector $\overrightarrow{M_s}$ defined by the minimum of the free energy, which leads to the following equations in spherical coordinates:

$$\frac{\partial F}{\partial \theta} = 0 \text{ and } \frac{\partial F}{\partial \varphi} = 0, \tag{4.2}$$

where θ and φ are the polar and azimuthal angles, the z-axis is directed perpendicularly to the plane of the sample. Solutions of (4.2) that minimize free energy F should be selected. Then, the ferromagnetic resonance condition for low dumping in spherical coordinates is given by the following equation under condition of equilibrium magnetization [38]:

$$\left(\frac{\omega}{\gamma}\right)^2 = \frac{1}{M_s^2 (\sin\theta)^2}\left\{\frac{\partial^2 F}{\partial \theta^2}\frac{\partial^2 F}{\partial \varphi^2} - \left(\frac{\partial^2 F}{\partial \theta\, \partial \varphi}\right)^2\right\}. \tag{4.3}$$

Taking partial derivatives in (4.3) with conditions (4.2), we find for the ferromagnetic resonance:

$$\left(\frac{\omega}{\gamma}\right)^2 = \left(H^r\cos(\theta^e-\theta^H) - 4\pi M_s\left(1-\frac{3N^{eff}}{4\pi}\right)\cos(2\theta^e)\right)\times$$

$$\times\left(H^r\cos(\theta^e-\theta^H) - 4\pi M_s\left(1-\frac{3N^{eff}}{4\pi}\right)\cos^2(\theta^e)\right), \quad (4.4)$$

with the condition from the first expression of (4.2) for polar angle:

$$H^r\sin(\theta^e-\theta^H) = 2\pi M_s\left(1-\frac{3N^{eff}}{4\pi}\right)\sin(2\theta^e), \quad (4.5)$$

where H^r is the magnitude of the ferromagnetic resonance field, θ^H and θ^e are the polar angles of $\overrightarrow{H^r}$ and magnetic moment at equilibrium respectively, ω is the frequency of the AC magnetic field and γ is the gyromagnetic ratio. Transcendental equations (4.4) and (4.5), in general case, do not admit solution for H^r in elementary functions and numerical calculation is required. Figure 4.3 shows the dependence of the resonance field H^r on the angle θ^H numerically calculated from (4.4) and (4.5) along with the experimental FMR data obtained from the continuous 60nm thick permalloy film. Continuous permalloy film shows only one FMR peak when measured at various angles. This film was fabricated under the identical conditions as all the nanopatterned arrays in presented work.

A small systematic discrepancy between the experimental results for FMR in continuous 60nm thick film and the resonance filed calculated for the case $N^{eff} = 0$ (corresponds to the infinite plate) should be noted, see Figure 4.3. The error is the largest for small values of θ^H (DC bias filed oriented normally to the plane of the film). Such

error is likely due to the surface anisotropy at the boundary between the permalloy film and the tantalum seed layer [39]. In the case $N^{eff} = \frac{4\pi}{3}$ that corresponds to magnetic isotropy: $N_x = N_y = N_z = \frac{4\pi}{3}$, the resonance field amplitude H^r does not depend on the orientation of the field, as expected. In our calculations we used gyromagnetic ratio value $g = 2.0023$. Saturation magnetization was determined from the fit of the model for continuous permalloy film: $\mu_0 M_s \approx 0.86$ T. Obtained value is close to the values reported in literature.

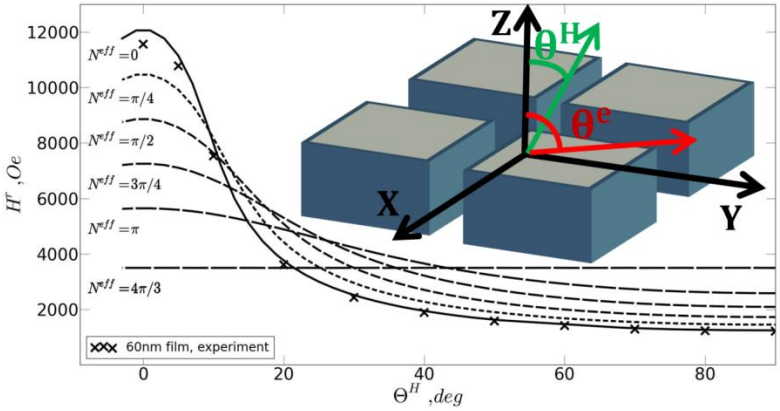

Figure 4.3 Resonance peak position H^r vs. field orientation, calculated for several values of the effective in-plane demagnetizing factor N^{eff}.

Calculations presented on the Figure 4.3 were performed for the frequency of AC magnetic field $\omega = 9.8$GHz. The same excitation frequency was used in the experiments. The inset shows the geometry of the system with coordinate system used in calculations and micromagnetic modeling as well as notation used in this report. Points marked with "X" are the experimentally measured values of H^r obtained for 60nm thick permalloy film, e-beam evaporated on top of 10nm Ta seed layer.

Comparing Figure 4.2 and Figure 4.3, it can be noted that experimentally observed lattice and shape modes can be distinguished using different values of the effective demagnetizing factor N^{eff}. In this approach, the lattice mode is characterized by

the low values of $N^{eff} \approx 0$ and for the shape mode $N^{eff} \approx \frac{19\pi}{18}$, see Figure 4.2. Low values of N^{eff} correspond to the planar symmetry, characteristic for coupled 2D arrays or continuous film and high IP anisotropy. Therefore, the name choice for resonance modes with low N^{eff} is lattice modes. Contrary, values of $N^{eff} \approx \frac{4\pi}{3}$ correspond to the highly symmetric case of a shape that is close to a sphere or a cube and give the name for the shape modes that have low dependence on the orientation of the bias magnetic field.

4.6 Micromagnetic Simulations

To characterize the magnetic states assumed to be responsible for the observed FMR modes, micromagnetic calculations were used to study the nonuniform magnetization in arrays of cubic permalloy nanomagnets with 60nm side length. In our simulations, rectangular cells with side length in range from 3 to 5 nm depending on the geometry of the system were used; damping parameter was set $\alpha = 1$ and gyromagnetic ratio $\gamma = 17.6$ MHz/Oe. Saturation magnetization used in our simulations $\mu_0 M_s \approx 0.86$ T was determined from the measurement of continuous permalloy film, deposited under the same conditions as the nanostructures.

We begin the micromagnetic analysis by examining the magnetization configuration at remanence. While remanent states are not directly related to the observed FMR spectrum, this information is useful for understanding the effects of intermagnet coupling on the magnetic texture inside the nanomagnets arranged in closely packed arrays, see Figure 4.4.

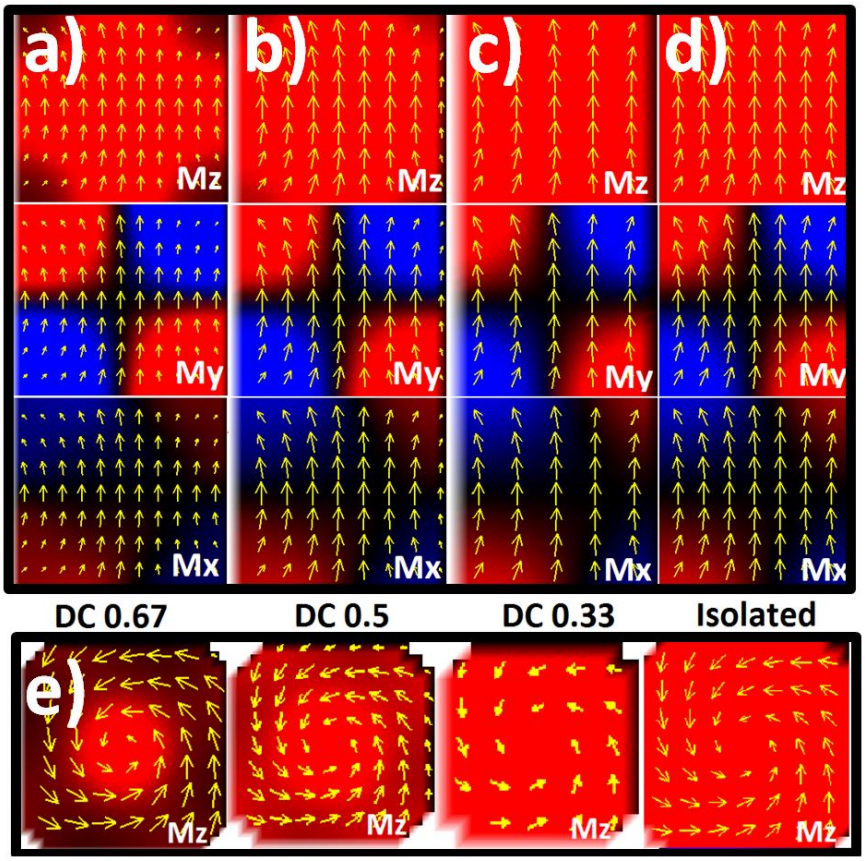

Figure 4.4 Spatial distribution of magnetization in rectangular nanomagnets arranged in square arrays with duty cycle: a) 0.67, b) 0.5, c) 0.33 and d) isolated nanomagnet without neighbors.

The top segment of the Figure 4.4 shows the cross sections in the XZ plane (see inset of the Figure 4.3) through the center of a nanomagnet and parallel to its vertical facet. The bottom row segment e) shows the cross sections at the bottom of nanomagnets parallel to XY plane. The background color intensity represents the magnetization components that are denoted at the bottom right corners (red – parallel to the corresponding axis, blue – antiparallel, black - zero). The arrows show the projection of the magnetization vectors on the plane of cross section. Corners of nanopillars are

rounded to better represent the actual shape observed in SEM images. The initial magnetic state in presented simulations was chosen to be saturated along Z axis.

While the topology of magnetic textures is similar for all three arrays with different duty cycles (Figure 4.4 columns (a), (b), (c) and isolated nanomagnet (Figure 4.4, column (d), the differences in magnetization distribution can also be observed. It should be noted that magnetization in the most densely packed array (Figure 4.4, top segment, column (a) is the most non-uniform comparing to the less dense arrays. This is especially noticeable at the corners and the facets of nanomagnets. Besides that, from Figure 4.4, bottom segment (e) it can be seen that localization of the vortex core (bright red color) pointing in the +Z direction gradually fades as duty cycle is decreased. Magnetization pattern of the least dense array is the closest to that of the isolated nanomagnet indicating decrease of coupling, as expected, see Figure 4.4, top segment, columns (c) and (d).

Micromagnetic simulations show that topology of the magnetic texture in cubic nanomagnets strongly depends on the magnitude and direction of the external bias field as well as on the spacing between the nanomagnets, Figure 4.5 and Figure 4.6. In this case, uniform and vortex-like magnetic textures can be observed. The effect of magnet-to-magnet separation is especially well seen from the comparison of the columns (a) and (b) of the Figure 4.6.

Consider the inset in the Figure 4.3. As the bias field direction is varied from OOP to IP in ZY plane, the highly nonuniform dipolar stray field from the neighboring along Y axis nanopillars changes direction from antiparallel to parallel to the magnetization of a nanomagnet under consideration. Non-uniformity of the effective field

and magnetization of nanomagnets is likely responsible for the presence of several ferromagnetic resonance modes, observed experimentally and nonuniform magnetization texture seen in microagnetic simulations.

Magnetization structure of the arrays with various duty cycles is similar for the cases of 1 kOe external field applied OOP and IP (not shown in this report). In these cases magnetization is presented by magnetic vortices with axes directed OOP or IP respectively. The more interesting case is of the bias magnetic field applied at an angle to the major axes of symmetry of the system, considered in more details below.

Figure 4.5 shows magnetization texture of the arrays with different duty cycles magnetized by 1 kOe bias field applied at the polar angle $\theta^{H} = 30^{\circ}$ in ZY plane.

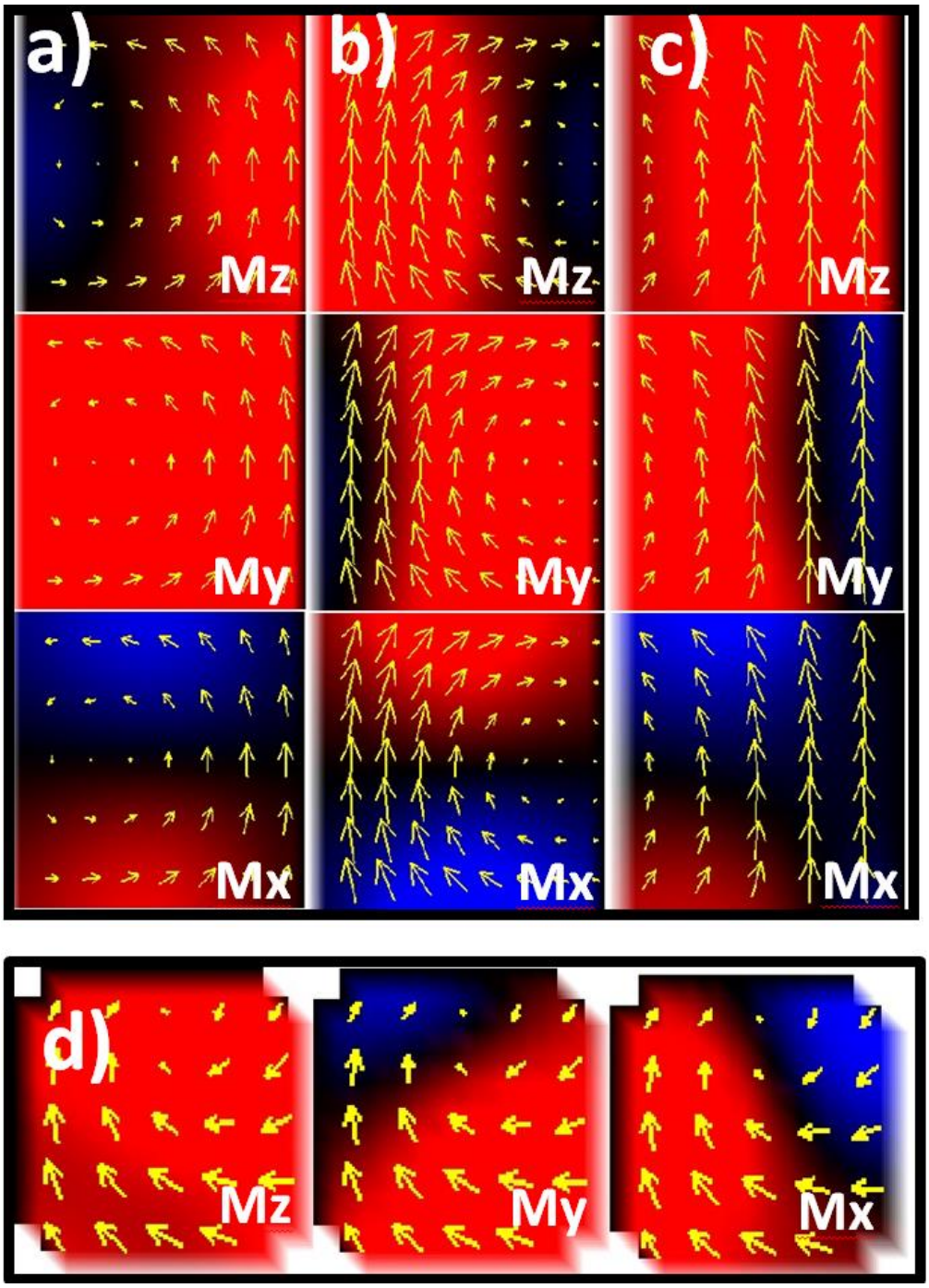

Figure 4.5 Spatial distribution of magnetization in cubic nanomagnets arranged in square arrays with duty cycle: column a) 0.67, b) 0.5 and c) 0.33. In this case, 1 kOe external filed applied at $\theta^{H} = 30^{\circ}$ to the normal of the arrays.

The sub-plots of the Figure 4.5, the columns a), b) and c), are the cross sections in the XZ plane (see the inset of the Figure 4.3) through the centers of nanomagnets and parallel to their vertical facets.

The bottom row segment d) of the Figure 4.5 shows magnetization texture of the array with duty cycle 0.33 considered at the XY plane at the base of a nanomagnet. The color coding is identical to the Figure 4.4 and shows amplitudes of three magnetization components M_x, M_y and M_z. For the calculations presented here, the initial magnetic state of each voxel was chosen to be random.

Magnetization of the samples with duty cycles 0.67 and 0.5, Figure 4.5 (a) and (b) respectively, is rather non-uniform and is represented by vortices with cores directed along Y axis. In contrast, the sample with duty cycle 0.33, Figure 4.5 (c), shows near-uniform magnetization along Z axis. More careful analysis of the cross sections of the magnetization structure in the sample with duty cycle 0.33, Figure 4.5, bottom segment (e), viewed in XY plane, reveals magnetic state that is represented by asymmetric vortex-like texture with the vortex core oriented along Z axis.

Topologically similar magnetic structures were observed in micromagnetic simulations performed for the samples magnetized by 1 kOe bias field applied at the angle $\theta^H = 60^\circ$ in ZY plane, see Figure 4.6. The exception in this case was the most densely packed array with duty cycle 0.67, Figure 4.6 column (a). Under these conditions, the magnetization is very close to uniform along the Y axis. Further analysis of the magnetization texture in this array viewed at different cross sections confirms the absence of vortex-like states in this sample. The arrays with duty cycles 0.5 and 0.33,

Figure 4.6 columns (b) and (c) respectively, demonstrate similarity to the case of $\theta^{H} = 30^{\circ}$. Here we observe vortex-like textures with vortex core directed along Y axis.

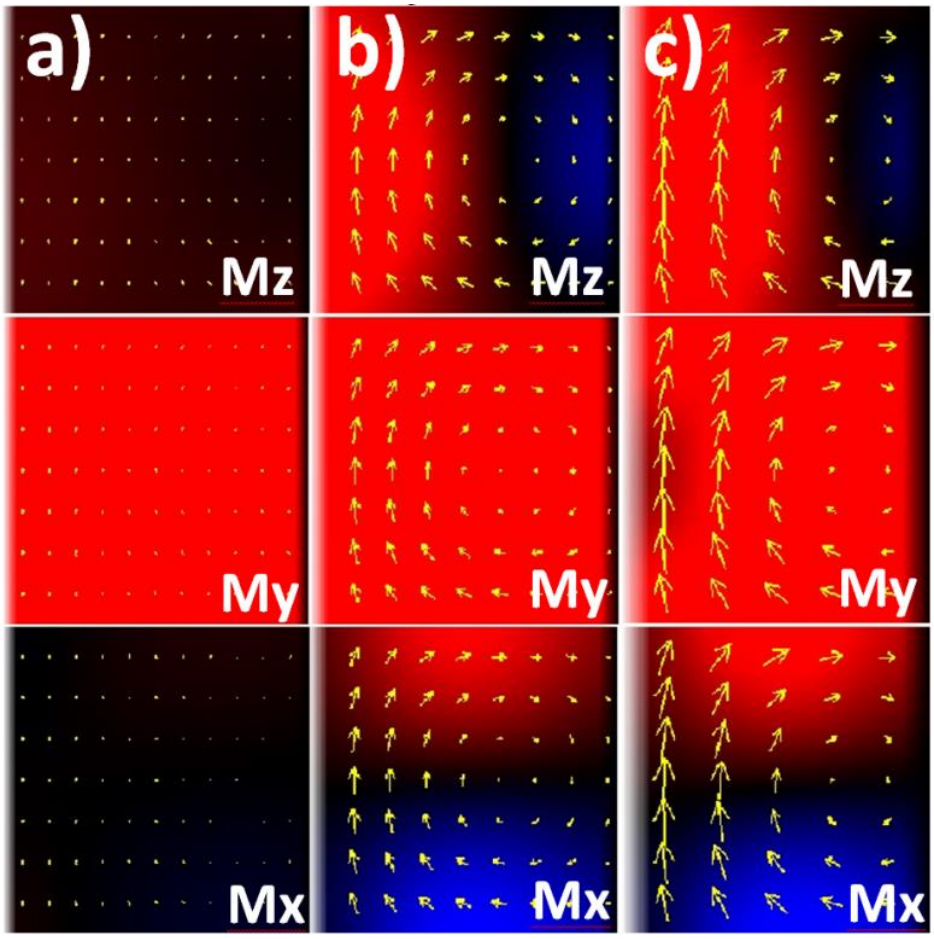

Figure 4.6 Spatial distribution of magnetization in cubic nanomagnets arranged in square arrays with duty cycle: a) 0.67, b) 0.5 and c) 0.33. Here 1 kOe bias field applied at the angle $\theta^{H} = 60^{\circ}$ to the normal to the plane of the arrays.

The sub-plots of the Figure 4.6 are cross sections in the XZ plane (see the inset of the Figure 4.3) through the centers of nanomagnets and parallel to their vertical facets. Color coding is identical to the Figure 4.4 and Figure 4.5. For the calculations presented here, the initial magnetic state of each cell was chosen to be random.

Nonuniform magnetization was observed in micromagnetic simulations for arrays in external bias field as high as 12 kOe. In that case the dominating component of

magnetization is directed along the applied field. Figure 4.7 shows projections of magnetization on vertical and horizontal cross section planes (rows (a) and (b) respectively) in the array with duty cycle 0.67 magnetized OOP by 12 kOe external field. It can be noted, that regions of nonuniform magnetization located at the top and bottom edges of nanomagnets. For the case of 12 kOe field simulations were run repeatedly with different initial magnetization directions assigned to each cell to examine different possible reversal paths and final states at 12 kOe. For all runs that included initial uniform magnetization along Z axis, vortex in XY plane and random magnetization of each cell, the final magnetization state was identical.

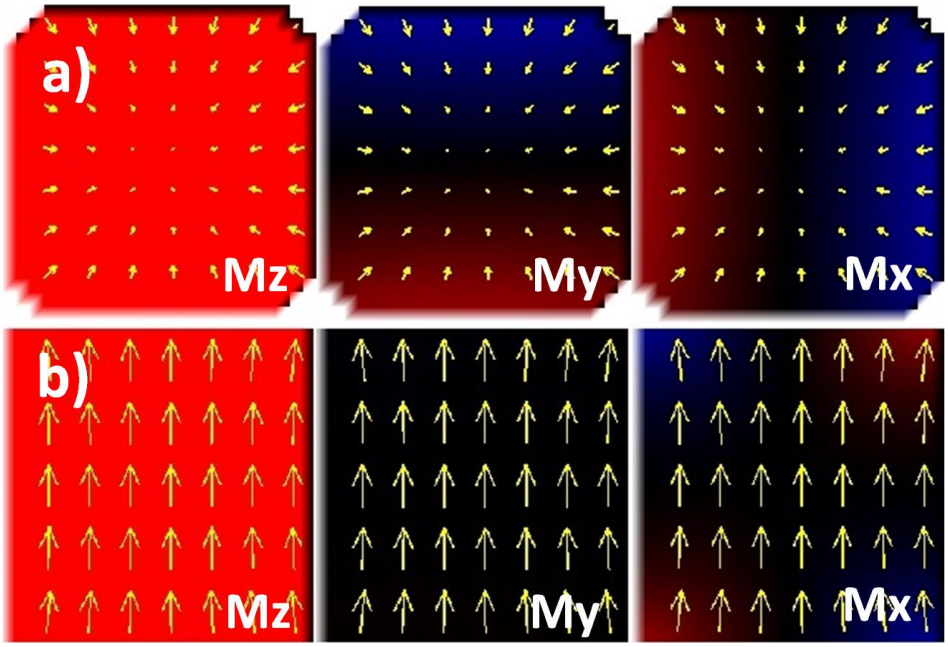

Figure 4.7 Spatial distribution of magnetization in 60nm cubic nanomagnets arranged in square lattice with duty cycle 0.67.

On the Figure 4.7, row a) shows magnetization projections taken at the horizontal cross section at the bottom of a nanomagnet. Row b) shows magnetization projections on

vertical cross section going through the central Z axis of a nanomagnet. Arrows and color coding are identical to the simulation figures above in the text.

Several simulation runs were performed for micromagnetic analysis. In case of zero applied field (remanent magnetization), calculated ground states of the system included vortices of different chirality and vortex core directions i.e. along X or Y axis, as expected due to the degeneracy of these states with respect to change of the X and Y axes. When the simulation unit cell included more than one nanomagnet, clusters/domains of nanomagnets with the same chirality were observed (not shown in this report). Besides chirality and vortex core orientation, all ground magnetic states in zero external field were topologically similar. In the presence of the external magnetic field, only difference in chirality of magnetization was observed.

4.7 Summary

To finalize this chapter, we measured the out-of-plane dependence of the FMR spectrum in square arrays of magnetostatically coupled cubic nanomagnets with side length of 60nm and center-to-center inter dot separation in range from 90nm to 180nm. Two dominant resonance modes (shape and lattice) were observed. We showed analytically that these modes can be characterized and distinguished using effective demagnetization factors N^{eff}. From analytical calculations $N^{eff} \approx 0$ corresponds to the lattice mode and $N^{eff} \approx \frac{19\pi}{18}$ represents the shape mode. Dependence of the resonance field magnitude on the angle of the bias field for these types of modes can be attributed to the symmetries of the lattice and to the shape of individual nanomagnets. Based on the effect of the interdot spacing on magnetic texture inside the nanomagnets and the value of

the effective demagnetizing factor we conjecture that highly angle dependent lattice mode is likely due to the presence of intermagnet coupling in the system.

From our experimental observations and numerical simulations, we conclude that structure of FMR spectrum and magnetization texture in arrays of cubic nanomagnets can strongly depend on the duty cycle of the arrays. Micromagnetic simulations further confirmed this assumption and suggested that magnetodynamic behavior in the systems presented in this report can be governed by the vortex-like magnetic textures inside the cubic nanomagnets. Our work shows that the structure of FMR spectrum and magnetic texture in nanomagnets can be effectively tuned by adjusting the geometrical parameters of nanodot arrays and utilizing highly non-uniform stray fields produced in the systems of closely packed sub-100nm magnets.

Chapter 5. Conclusions

We built and tested Ferromagnetic Resonance Spectrometer with variable direction of externally applied magnetic field. In our experimental setup we used a coplanar waveguide as high frequency field generator that induces resonant precession of magnetization in the investigated samples. This measurement technique proved to be an effective approach to characterize magnetodynamic properties of magnetic nanostructures as well as continuous films. Ability to apply the external bias field at various angles to the plane of the measured samples allowed for characterization of demagnetizing fields of the tested arrays as well as observation of the reach modal structure of the FMR spectrum. Unlike our experimental setup, conventional FMR measurements performed either with in-plane or out-of-plane bias field wouldn't provide the information about the evolution of the FMR spectrum with respect to the angle of the DC field. Collected data allowed us to gain insights into the factors that determine the FMR resonance spectrum in dipolarly coupled nanostructures.

Using electron beam lithography and lift-off technique we developed nanofabrication processes and prepared sets of 2D arrays of coupled permalloy nanodots with various geometrical parameters, interdot distance and 2D lattice types. While the height of nanodots in all of the fabricated and tested samples was kept the same and equal 60 nm, the lateral size was varied in the range from 60 nm to 400 nm. This approach allowed us to tune the shape anisotropy of individual nanomagnets in wide range of values. From our observations we can conclude that all three factors play significant role

in the collective magnetodynamic behavior of coupled nanodots: geometry of individual nanodot, interdot separation and arrangement of nanomagnets in a 2D lattice.

Our magnetostatic and magnetodynamic measurements suggest that dipolar coupling between nanomagnets plays significant role and induces the in-plane magnetic anisotropy in the system of closely packed magnetic nanodots. This can be concluded from analysis of the in-plane and out-of-plane hysteresis loops as well as evolution of FMR spectrum with respect to angle of the bias field, as shown in the Chapter 4. It is also likely that highly non-uniform dipolar field lifts FMR modes degeneracy and causes FRM resonance peaks to split.

Our analytic calculations suggest that two FMR modes observed in the square lattice arrays of 60 nm cubes can be distinguished by their effective demagnetizing factors. These demagnetizing factors represent two distinct symmetries of the system: local shape anisotropy of individual nanomagnets and 2D planar symmetry of the array.

While emergence of collective excitation modes is rather unwanted phenomenon in magnetic data storage systems it can play important role in magnetic metamaterials. From this perspective, our work identifies the key parameters and develops the approaches to tune magnetodynamic properties of magnetic metamaterials.

References

[1] “Perpendicular magnetic Recording Technology”, Hitachi Global Storage Technology, 2007

[2] Y.-W. Jun, J.-W. Seo, and J. Cheon, “*Nanoscaling laws of magnetic nanoparticles and their applicabilities in biomedical sciences*” Accounts of Chemical Research 2, (2008)

[3] J. C. Mallinson, “*A New Theory of Recording Media Noise*” IEEE Trans. Mag. 27, NO. 4, (1991)

[4] J.-G. Zhu, X. Zhu, and Y. Tang, “*Microwave Assisted Magnetic Recording*” IEEE Trans. Mag. 44, NO. 1, (2008)

[5] Thomas R. Albrecht, Hitesh Arora, Vipin Ayanoor-Vitikkate, Jean-Marc Beaujour, Daniel Bedau, David Berman, Alexei L. Bogdanov, Yves-Andre Chapuis, Julia Cushen, Elizabeth E. Dobisz, Gregory Doerk, He Gao, Michael Grobis, Bruce Gurney, Fellow, IEEE, Weldon Hanson, Olav Hellwig, Toshiki Hirano, Pierre-Olivier Jubert, Dan Kercher, Jeffrey Lille, Zuwei Liu, C. Mathew Mate, Yuri Obukhov, Kanaiyalal C. Patel, Kurt Rubin, Ricardo Ruiz, Manfred Schabes, Lei Wan, Dieter Weller, Tsai-Wei Wu, and En Yang, “*Bit-Patterned Magnetic Recording: Theory, Media Fabrication, and Recording Performance*” IEEE Trans. Mag. 51, NO. 5, (2015)

[6] Y. Kajiwara, K. Harii, S. Takahashi, J. Ohe, K. Uchida, M. Mizuguchi, H. Umezawa, H. Kawai, K. Ando, K. Takanashi, S. Maekawa and E. Saitoh, “*Transmission of electrical signals by spin-wave interconversion in a magnetic insulator*” Nature 464, (2010)

[7] D. W. Healy, "*Ferromagnetic Resonance in Nickel Ferrite as a Function of Temperature*" Phys. Rev. 86, 1009 (1952)

[8] L. Landau, E. Lifshitz, "*On the Theory of the Dispersion of Magnetic Permeability in Ferromagnetic Bodies*" Phys. Z. Sowjet. 8, 153-169 (1935)

[9] K. Yu. Guslienko, V. Novosad, Y. Otani, H. Shima, and K. Fukamichi, "*Magnetization reversal due to vortex nucleation, displacement, and annihilation in submicron ferromagnetic dot arrays*" Phys. Rev. B 65, 024414, (2001)

[10] A.V. Chumak, V.I. Vasyuchka, A. A. Serga, and B. Hillebrands, "*Magnon spintronics*" Nature Physics 11, 453–461 (2015)

[11] B. Lenk, H. Ulrichs, F. Garbs, M. Münzenberg, "*The building blocks of magnonics*" Phys. Rep. 507, 107–136 (2011)

[12] V. V. Kruglyak, S. O. Demokritov and D. Grundler, "*Magnonics*" J. Phys. D: Appl. Phys. 43, 264001 (2010)

[13] A. V. Chumak, A. A. Serga, B. Hillebrands, "*Magnon transistor for all-magnon data processing*" Nature Communications 5, 4700 (2014)

[14] Arabinda Haldar, Dheeraj Kumar, and Adekunle Olusola Adeyeye, "*A reconfigurable waveguide for energy-efficient transmission and local manipulation of information in a nanomagnetic device*" Nature Nanotechnology 11, 437–443 (2016)

[15] Arabinda Haldar and Adekunle Olusola Adeyeye, "*Artificial metamaterials for reprogrammable magnetic and microwave properties*" App. Phys. Lett. 108, 022405 (2016)

[16] Marc Vogel, Andrii V. Chumak, Erik H. Waller, Thomas Langner, Vitaliy I. Vasyuchka, Burkard Hillebrands, and Georg von Freymann, "*Optically reconfigurable magnetic materials*" Nature Physics 11, 487–491 (2015)

[17] Mehrdad Elyasi, Charanjit S. Bhatia, and Hyunsoo Yang, "*Magnetization reversal using excitation of collective modes in nanodot matrices*" Sci. Rep. 5, 7908 (2015)

[18] Nissim Amos, John Butler, Beomseop Lee, Meir H. Shachar, Bing Hu, Yuan Tian, Jeongmin Hong, Davil Garcia, Rabee M. Ikkawi, Robert C. Haddon, Dmitri Litvinov, Sakhrat Khizroev, "*Multilevel-3D Bit Patterned Magnetic Media with 8 Signal Levels Per Nanocolumn*" PLoS ONE 7, 7 (2012)

[19] S.O. Demokritov, B. Hillebrands, A.N. Slavin, "*Brillouin light scattering studies of confined spin waves: linear and nonlinear confinement*" Physics Reports 348, 6 (2001)

[20] Justin M. Shaw, T. J. Silva, Michael L. Schneider, Robert D. McMichael, "*Spin dynamics and mode structure in nanomagnet arrays: Effects of size and thickness on linewidth and damping*" Phys. Rev. B 79, 184404 (2009)

[21] H. T. Nembach, Justin M. Shaw, T. J. Silva, W. L. Johnson, S. A. Kim, R. D. McMichael, P. Kabos, "*Effects of shape distortions and imperfections on mode frequencies and collective linewidths in nanomagnets*" Phys. Rev B 83, 094427 (2011)

[22] Roman Verba, Gennadiy Melkov, Vasil Tiberkevich and Andrei Slavin, "*Collective spin-wave excitations in a two-dimensional array of coupled magnetic nanodots*" Phys. Rev. B 85, 014427 (2012)

[23] Ivan Lisenkov, Vasyl Tyberkevych, Andrei Slavin, Pavel Bondarenko, Boris A. Ivanov, Elena Bankowski, Thomas Meitzler, and Sergey Nikitov, "*Spin-wave edge modes in finite arrays of dipolarly coupled magnetic nanopillars*" Phys. Rev. B 90, 104417 (2014)

[24] Ryuichi Shindou, Ryo Matsumoto, Shuichi Murakami, and Jun-ichiro Ohe, "*Topological chiral magnonic edge mode in a magnonic crystal*" Phys. Rev. B 87, 174427 (2013)

[25] G. Gubbiotti, M. Conti, G. Carlotti, P. Candeloro, E. Di Fabrizio, K. Yu. Guslienko, A. Andre, C. Bayer, and A. N. Slavin, "*Magnetic field dependence of quantized and localized spin wave modes in thin rectangular magnetic dots*" J. Phys.: Condens. Matter 16 7709–7721 (2004)

[26] K.Y. Guslienko, Y. Kobljanskyj, G.A. Melkov, V. Novosad, S.D. Bader, M. Kostylev, A.N. Slavin, "*Nonlinear spin waves in two dimensional arrays of magnetic nanodots*" Ultrafast Magnetism I, Springer Proceedings in Physics, v. 159, 206-209 (2014)

[27] Han-Jong Chia, Feng Guo, L. M. Belova, and R. D. McMichael, "*Nanoscale Spin Wave Localization Using Ferromagnetic Resonance Force Microscopy*" Phys. Rev. Lett. 108, 087206 (2012)

[28] Bivas Rana, Dheeraj Kumar, Saswati Barman, Semanti Pal, Yasuhiro Fukuma, YoshiChika Otani, and Anjan Barman, "*Detection of picosecond magnetization dynamics of 50 nm magnetic dots down to the single dot regime*" ACS Nano, 5, 9559 (2011)

[29] H. T. Nembach, J. M. Shaw, C. T. Boone, and T. J. Silva, "*Mode- and size-dependent Landau-Lifshitz damping in magnetic nanostructures: Evidence for nonlocal damping*" Phys. Rev. Lett. 110, 117201 (2013)

[30] X. Zhou, D. Kumar, I. S. Maksymov, M. Kostylev, and A. O. Adeyeye, "*Axially and radially quantized spin waves in thick permalloy nanodots*" Phys. Rev. B 92, 054401 (2015)

[31] H.-J. Chia, F. Guo, L. M. Belova, and R. D. McMichael, "*Spectroscopic defect imaging in magnetic nanostructure arrays*" Appl. Phys. Lett. 101, 042408 (2012)

[32] Susmita Saha, Ruma Mandal, Saswati Barman, Dheeraj Rumar, Bivas Rana, Yasuhiro Fukuma, Satoshi Sugimoto, YoshiChika Otani, and Anjan Barman, "*Tunable Magnonic Spectra in Two-Dimensional Magnonic Crystals with Variable Lattice Symmetry*" Adv. Funct. Mater. 23, 2378–2386 (2013)

[33] Susmita Saha, Saswati Barman, Satoshi Sugimoto, YoshiChika Otanibc and Anjan Barman, "*Tunable picosecond spin dynamics in two dimensional ferromagnetic nanodot arrays with varying lattice symmetry*" RSC Adv., 5, 34027–34031 (2015)

[34] Ivan Lisenkov, Vasyl Tyberkevych, Sergey Nikitov, and Andrei Slavin, "*Theoretical formalism for collective spin-wave edge excitations in arrays of dipolarly interacting magnetic nanodots*" Phys. Rev. B 93, 214441 (2016)

[35] M. Pardavi-Horvath, B. G. Ng, F. J. Castaño, H. S. Körner, C. Garcia and C. A. Ross, "*Angular dependence of ferromagnetic resonance and magnetization configuration of thin film Permalloy nanoellipse arrays*" J. Appl. Phys. 110, 053921 (2011)

[36] M. R. Scheinfein, LLG Micromagnetics Simulator, software for micromagnetic simulations, http://llgmicro.home.mindspring.com

[37] S. L. Vysotskiia, S. A. Nikitov, Yu. A. Filimonova, and Yu. V. Khivintsev, "*Hybridization of Spin-Wave Modes in a Ferromagnetic Microstrip*" JETP Lett. 88, 7, pp. 461–465 (2008)

[38] H. Suhl, "*Ferromagnetic Resonance in Nickel Ferrite Between One and Two Kilomegacycles*" Phys. Rev. 97, 555 (1955)

[39] James O. Rantschler, P. J. Chen, A. S. Arrott, R. D. McMichael, W. F. Egelhoff Jr., and B. B. Maranville, "*Surface anisotropy of permalloy in NM/NiFe/NM multilayers*" J. Appl. Phys. 97, 10J113 (2005)